ADVANCED ENGINEERING MATERIALS
www.aem-journal.com

Latest Advances in Manufacturing and Machine Learning of Bulk Metallic Glasses

Olivia A. Graeve, Mireya S. García-Vázquez,* Alejandro A. Ramírez-Acosta, and Zachary Cadieux*

In this review, two interrelated areas are focused on for the development of novel amorphous metallic alloys, namely, materials processing and machine learning techniques for the design of new alloy compositions. Findings, barriers, and opportunities are described, targeting powder production and sintering, additive manufacturing, and postprocessing techniques, followed by the latest developments in artificial intelligence algorithms for both the design of new alloys and for alloy classification tasks.

1. Introduction

Amorphous metal alloys (i.e., metallic glasses) are of great technological interest because they exhibit a variety of unique properties, including a very large elastic limit because of the lack of dislocations that induce plastic deformation[1] and high resistance to corrosion and wear because of the lack of grain boundaries,[2,3] among many other useful properties. Thus, a number of reviews have been written on these materials, including some early reviews that effectively describe foundational issues related to the thermodynamics and kinetics of these types of alloys,[4–7] applications in cutting tools and gears,[8,9] medical implants,[10–13] space technologies,[14] structural components,[15] wastewater treatment,[16] catalysis,[17,18] and countless others.[19] As new applications are recognized and explored, research efforts to improve the processing and manufacturing of metallic glasses continue to be of interest,[20–24] resulting in a myriad of patents and patent activity.[25] Owing to their extraordinary properties, the application of these alloys in extreme environments, for example in environments of higher temperature, is very relevant, but difficult because most of these alloys crystallize at relatively low temperatures. Thus, the development of metallic glasses with crystallization temperatures higher than 700 °C[26] is desirable and is resulting in intense research efforts. A search for metallic glasses that function at cryogenic temperatures,[27,28] that can be manufactured and can function in space environments,[29] and that resist radiation[30–35] and high pressures[36,37] is also of great interest. This review covers two areas of critical importance for the continued development of metallic glasses, namely, 1) processing techniques that can allow the manufacturing of new compositions both in powder and bulk form; and 2) the use of emerging artificial intelligence techniques for predicting new materials compositions.

O. A. Graeve, Z. Cadieux
Department of Mechanical and Aerospace Engineering
University of California San Diego
9500 Gilman Drive - MC 0411, La Jolla, CA 92093-0411, USA
E-mail: ograeve@ucsd.edu

M. S. García-Vázquez, A. A. Ramírez-Acosta
Centro de Investigación y Desarrollo de Tecnología Digital
Instituto Politécnico Nacional
Av. Instituto Politécnico Nacional No. 1310, Tijuana, Baja California
C.P. 22435, Mexico
E-mail: msarai@ipn.mx

The ORCID identification number(s) for the author(s) of this article can be found under https://doi.org/10.1002/adem.202201493.

DOI: 10.1002/adem.202201493

2. Manufacturing Approaches

There are two main approaches for manufacturing bulk metallic glass (BMG) components: 1) production directly from melt, such as melt casting into a mold; and 2) production from powders, such as 3D printing and embossing methods. The powders themselves can be produced using techniques such as gas atomization, in which droplets of molten metal are rapidly cooled using a high-pressure jet of gas, generally resulting in well-dispersed powders, as illustrated in **Figure 1** for two types of amorphous alloys.[38,39] A general diagram listing the main approaches for the manufacturing of these types of materials is provided in **Figure 2**. In this review, we will broadly describe manufacturing techniques from a melt, to provide completeness to the discussion, but without progressing into details, because the techniques are very well known and utilized.[40] We will present a more thorough discussion of techniques that commence with powders, which represent newer technologies and significant challenges are still present. They include advanced manufacturing (i.e., 3D printing) techniques and state-of-the-art metallurgical approaches. Discussion of postprocessing techniques, including welding and machining, will also be presented.

2.1. Manufacturing from a Melt

There are multiple ways of manufacturing BMGs from a melt. The two primary methods are casting into a mold or melt spinning. As input products, both require elemental precursors that are typically arc melted,[41] usually in vacuum or argon-rich environments, to create a master alloy, which is then remelted to achieve homogeneous mixing. The melt is then either cast or

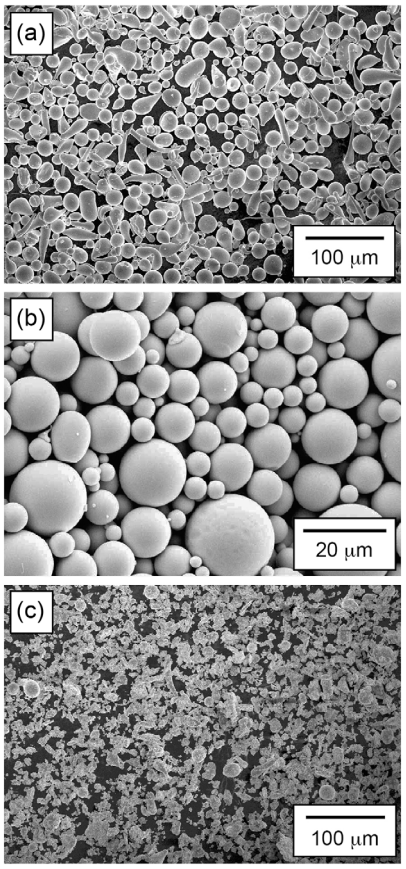

Figure 1. Scanning electron micrographs of gas atomized powders of a) $Fe_{48}Mo_{14}Cr_{15}Y_2C_{15}B_6$,[38] b) $Ni_{53}Nb_{20}Ti_{10}Zr_8Co_6Cu_3$,[39] and c) $Fe_{48}Mo_{14}Cr_{15}Y_2C_{15}B_6$ after high-energy ball milling.[38] Reproduced with permission.[38] Copyright 2018, Elsevier. Reproduced with permission.[39] Copyright 2006, Taylor and Francis.

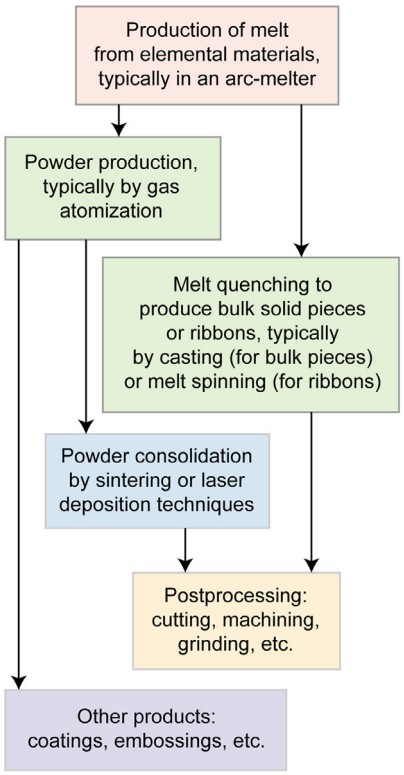

Figure 2. Typical processes for the manufacturing of amorphous metal products.

spun to produce the final BMG product. Instrumentation that combines the arc melting process with casting are described in the literature and can result in specimens of many compositions.[42]

A typical example of a mold casting process is described for the manufacturing of rods, with a specific example illustrated in **Figure 3**a for $Fe_{60}Cr_{10}Mo_9C_{10}B_6Er_2Ni_3$.[43] Here, industrial-grade powders of Fe, Cr, Mo, C, B, Er, and Ni are first melted and remelted in an arc furnace, and then cast into a water-cooled copper mold, resulting in rods of 5–10 mm in diameter and lengths of approximately 5–6 cm. The amorphous character of the specimens is evident from the X-ray diffraction patterns of Figure 3b for alloys $Fe_{60}Cr_{10}Mo_9C_{10}B_6Er_2Ni_3$, $Fe_{65}Cr_9Mo_8C_{10}B_6Er_2$, and $Fe_{60}Cr_{10}Mo_9C_{13}B_6Er_2$. However, while rods and other simple shapes can be produced, the technique has limitations. Complicated shapes that are hollow or have sharp corners are not achievable because of gradients in cooling rate that can result in sections of a specimen that are amorphous and others that are crystalline. Modifications to the casting process that can inhibit nucleation and the undesirable formation of crystalline regions have been successfully explored. One such technique makes use of a DC current applied between the molten metal and the mold, which modifies the surface tension of the melt and avoids inhomogeneous solidification.[44] Another issue is that for most alloys the casting process must be executed in an inert atmosphere to prevent oxygen contamination, although some compositions have been developed that resist oxidation and can be cast in air. For example, $Fe_{44}Mn_{11}Cr_{10}Mo_{12}C_{15}B_6Ho_2$[45] can be produced in the form of 6 mm diameter rods in air using a copper mold and commercial-grade elemental powders, with the oxidation resistance imparted by the presence of holmium that forms a holmium oxide surface coating and protects the inside of the rods.

Under some circumstances, the production of partially crystalline specimens is desired to improve toughness or other properties. The case of $Cu_{43}Zr_{43}Al_7Be_7$[46] is one example among many in the preparation of what are described as in situ bulk metallic glass composites that contain nanocrystalline phases. These specimens were prepared by first arc-melting high purity elemental powders in a Ti-gettered argon atmosphere and subsequently casting the melt in a water-cooled copper mold of 3 mm diameter. Variation in cooling rate was achieved by increasing the mass of melt poured into the mold and by annealing sections of the as-cast rods at a temperature of 682 K for 3 min. Cooling rate can also be varied by casting into wedge-shaped copper molds, resulting in some regions that are crystalline and some that are amorphous, as illustrated in **Figure 4** for the case of a $Mg_{84}Ni_{10}Gd_6$ alloy at various thicknesses (Z) across the wedge.[47]

Beyond the rods produced by casting, other shapes can also be manufactured from a melt, such as the formation of wires or ribbons of a variety of dimensions and compositions. Several

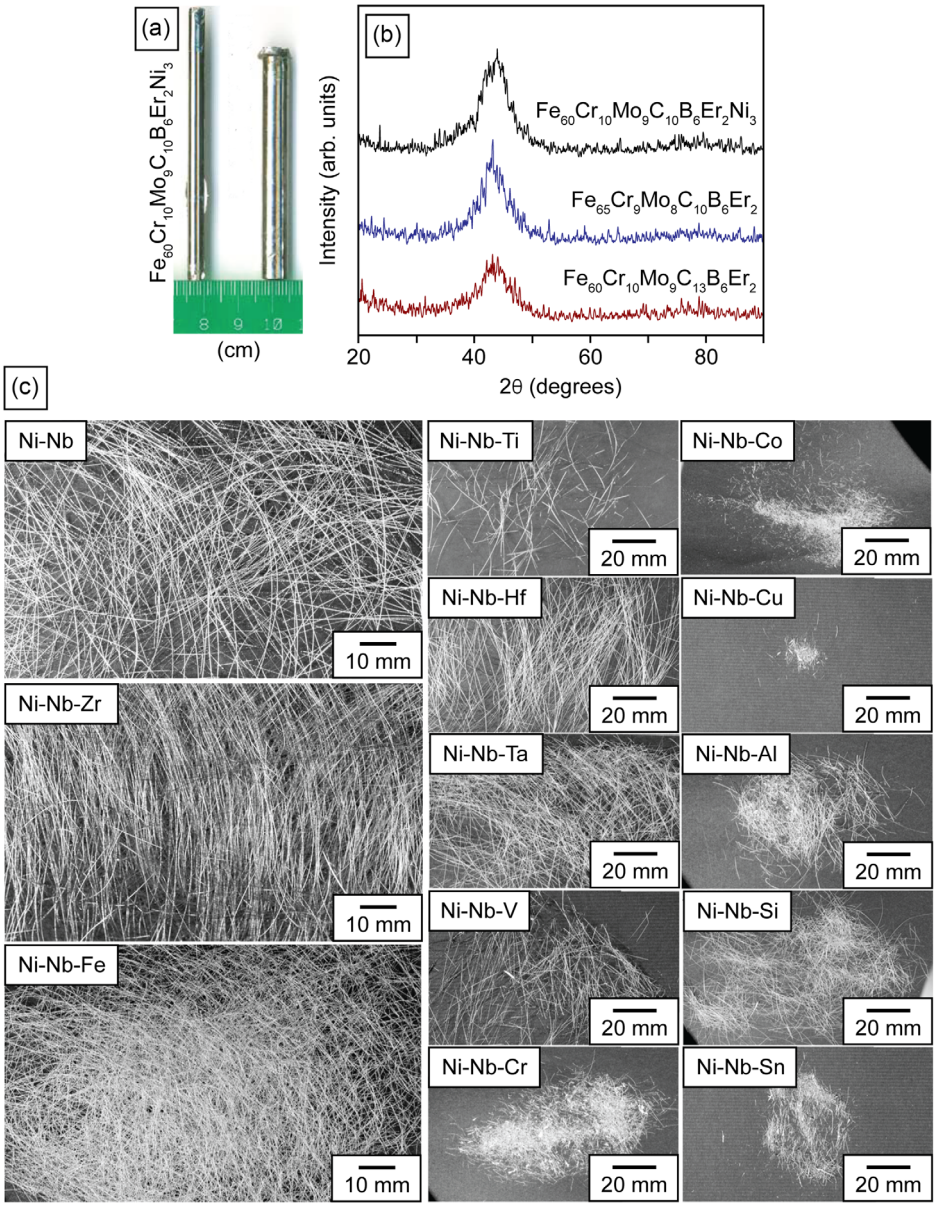

Figure 3. a) $Fe_{60}Cr_{10}Mo_9C_{10}B_6Er_2Ni_3$ rods of 5 and 8 mm in diameter and b) X-ray diffraction patterns of three Fe-based amorphous alloys of 8 mm in diameter. Reproduced with permission.[43] Copyright 2006, Elsevier. c) Melt-extracted $Ni_{60}Nb_{20}M_{20}$ alloy wires with M = Ti, Zr, Hf, V, Nb, Ta, Cr, Fe, Co, Cu, Al, Si, and Sn. Reproduced with permission.[48] Copyright 2009, Elsevier.

examples are provided in Figure 3c for Ni–Nb-based alloys.[48] Here, the melt is quenched by pouring drops of the alloy into a spinning copper wheel while the wheel is rotating at high speed. This melt spinning process is an excellent way to produce large amounts of thin ribbons such as $Mg_{67}Zn_{28}Ca_5$ (thickness = 106 μm),[49] $(Ni_{0.6}Nb_{0.4})_{45}Zr_{50}Co_5$ (thickness = 50 μm; width = 20 mm),[50] $Fe_x(P_{10}C_9Si)_{5-0.05x}$ ($x = 76-82$),[51] $Co_{65.5}Si_{18}B_{10}Cr_{6.5}$, and $Co_{65.5}Si_{18}B_{10}Fe_{6.5}$,[52] among many others, as well as wires.[53–55] Melt spinning tends to have a much higher cooling rate than mold casting, which allows for continuous production that makes large-scale production efficient and simple.

Finally, thermoplastic forming, also referred to as hot embossing, is a newer net-shaping technique used primarily for the fabrication of small-scale components, although larger components are also achievable. The technique is versatile for the manufacturing of complex geometries and is described in detail in the review by Ni et al.[56] A primary consideration for effective implementation is the superplastic deformation capacity of metallic glasses in the supercooled liquid state (between the glass transition and crystallization temperatures). Thus, here the alloy is not molten, but in a highly viscous state. This brings its own challenges, namely, the risk of devitrification when the alloy is held above the glass transition temperature, which increases

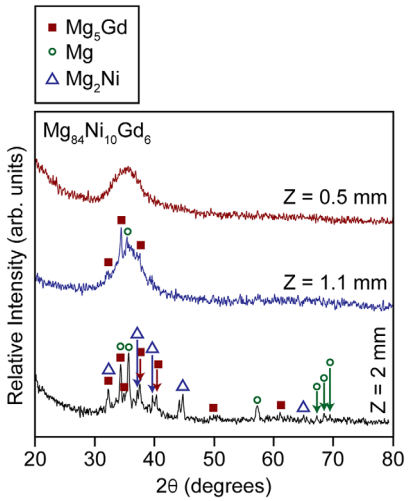

Figure 4. X-ray diffraction patterns obtained from cross sections of a $Mg_{84}Ni_{10}Gd_6$ wedge at thicknesses of 0.5, 1.1, and 2 mm across the wedge. Reproduced with permission.[47] Copyright 2013, The Minerals, Metals & Materials Society and ASM International.

as processing time and temperature increase, as well as issues of oxidation at higher temperatures. Also, the technique continues to have limitations in fabricating highly complex structures, thus advanced manufacturing processes (to be discussed later) are receiving significant attention, as they are perhaps better equipped to resolve this issue.

A specific example[57] of the hot embossing process for a gear of $Zr_{65}Cu_{17.5}Ni_{10}Al_{7.5}$ involves the preparation of rods (diameter = 3 mm) by arc melting and casting, which are then subsequently sliced into specimens of 0.6 mm height. These specimens are then heated to the superplastic temperature and pressed into a silicon mold (shown in **Figure 5**a). Wang et al.[57] found optimal conditions of 683 K embossing temperature, $0.001\,s^{-1}$ strain rate, 2776 s incubation time (time the sample is heated to the embossing temperature before applying load), and 880 s forming time (time the sample is compressed into the mold), resulting in the specimen shown in Figure 5b. The silicon mold was later removed by dissolving in 40% KOH solution at a temperature of 353 K. Examples of other shapes prepared by similar processes are found for $Zr_{41.2}Ti_{13.8}Cu_{12.5}Ni_{10}Be_{22.5}$,[58] $Mg_{58}Cu_{31}Y_{11}$,[59] $Pt_{57.5}Cu_{14.7}Ni_{5.3}P_{22.5}$,[60] and $Ni_{53}Nb_{20}Zr_8Ti_{10}Co_6Cu_3$,[61] among many others. A variation of this technique is molding using pressurized gas, analogous to silica glass blowing,[62] which results in remarkable curved shapes.[63]

2.2. Manufacturing from Powders

2.2.1. High-Energy Ball Milling

An initial step that may be necessary when manufacturing bulk samples involves a milling procedure of the powders or ribbons,[64,65] which is used to reduce dimensions (i.e., particle size) or to vitrify crystalline powders. Vitrification of powders is possible because of the continuous and, in some cases, very high impact energies the powders experience during the process,

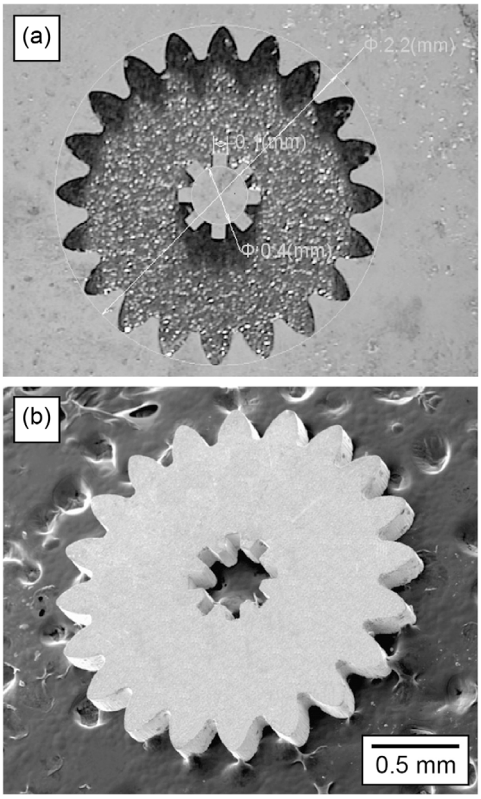

Figure 5. a) Optical micrograph of silicon mold and b) resulting microgear of $Zr_{65}Cu_{17.5}Ni_{10}Al_{7.5}$. Reproduced with permission.[57] Copyright 2009, Elsevier.

which can eventually cause atomic disorder. Figure 1c shows milled powders of $Fe_{48}Mo_{14}Cr_{15}Y_2C_{15}B_6$, obtained by planetary ball milling of the powders in Figure 1a.[38] Here, the experimental parameters include a speed of 400 rpm of the main disk, 2 h of milling, and ball-to-powder ratio of 10:1. The reduction in particle size is evident from the micrographs. Weeber and Bakker[66] describe in detail the case of vitrification of powders from crystalline precursors. Processing details and relevant parameters on the ball milling technique can be found in the general reviews by Koch,[67] Taha et al.,[68] Gilman and Benjamin,[69] Mucsi,[70] Murty and Ranganathan,[71] Sundaresan and Froes,[72] Suryanarayana,[73] Enayati and Mohamed,[74] and Seshan and Kaneko.[75] The literature on this technique is vast and the reader can find many specific details within each of the latter reviews.

2.2.2. Sintering

Initial attempts at producing bulk metallic glasses from amorphous powders involved the use of the hot-pressing technique.[76] However, because of the higher temperatures necessary to obtain fully dense specimens, the powders devitrified significantly or completely. An early example of this is described by Inoue et al.,[77] where powders of $Fe_{58}Cr_{16}Mo_8C_{18}$ were manufactured by gas atomization and size-separated by sieving into powders smaller than 24 μm, between 24 and 36 μm, between 36 and 44 μm, and above 44 μm. Only the powders smaller than

24 μm were determined to be amorphous and pressed into dense cylindrical specimens of 10 mm in diameter and 8 mm in height. With sintering time and pressure set at ≈26.7 min and 62.4 MPa, respectively, and sintering temperatures ranging from 1053 to 1403 K, all specimens resulted in mixed crystalline phases consisting mostly of α-Fe (ferrite) and metal carbide phases, even at the lowest sintering temperature of 1053 K. Thus, hot-pressing is not advantageous for obtaining dense metallic glass specimens. There are some processes one can implement to reduce and/or eliminate devitrification, namely, one can reduce the particle size (i.e., increase the surface area) of the powders to reduce the sintering temperature below the glass transition temperature of the alloy. For a copper-based amorphous alloy of composition $Cu_{44}Nb_{42}Si_{14}$ obtained by mechanical alloying, particle sizes in the range of 200–500 nm were obtained,[78] resulting in a mostly amorphous specimen when sintering at 673 K. Nonetheless, a (111) crystalline peak of copper was still present in the X-ray diffraction pattern, showing that the hot-pressing process was still not fully successful.

An essential parameter during hot-pressing is the pressure itself.[79] The limitations of lower pressures are evident from hot-pressing $Al_{85}Y_8Ni_5Co_2$ at pressures of 150–340 MPa and temperatures of 545–560 K, resulting in low relative densities of 80%.[80] For $Al_{85}Ni_9Nd_4Co_2$ samples, a relative density of 94% was obtained at a sintering temperature and pressure of 513 K and 700 MPa, respectively.[81] Contrast, the latter results with those obtained for $Co_{71}Ti_{24}B_5$ sintered at a higher pressure of 780 MPa and resulting in a relative density of 99.5%[82]; for $Ti_{60}Al_{15}Cu_{10}W_{10}Ni_5$ sintered at a pressure of 936 MPa and resulting in a relative density of 99.8%[83]; and for $Zr_{52}Al_6Ni_8Cu_{14}W_{20}$ sintered at a pressure of 936 MPa and resulting in a relative density of 99.82%.[84] For a pressure of 1.5 GPa, X-ray amorphous specimens of $Si_{55}Al_{20}Fe_{10}Ni_5Cr_5Zr_5$ (dimensions: 10 mm diameter and 4 mm height) of 98.3% relative density were obtained at a sintering temperature of 687 K.[85] A small increase in temperature to 708 K resulted in the presence of X-ray diffraction peaks, showing the sensitivity to temperature when sintering close to the 698 K crystallization temperature of this alloy. Thus, manufacturing outcomes can be improved when increasing pressure.

The selection of temperature is just as critical as pressure and always connected to the glass transition and crystallization temperatures of the alloy in question. Indeed, the ideal sintering temperature is one in between these two defining temperatures, known as the supercooled liquid region ($\Delta T = T_x - T_g$),[86] as this is the region when the alloy is minimally viscous, and the powders can deform optimally to achieve the highest relative densities. Alloys with wide supercooled liquid regions, such as $Ni_{57}Zr_{20}Ti_{20}Si_3$ ($\Delta T = 88$ K),[87] are best when defining conditions for sintering, as the large ΔT increases the temperature window for sintering that avoids crystallization. Alloys with narrower regions, such as $Mg_{49}Y_{15}Cu_{36}$ ($\Delta T = 46$ K),[88] $Mg_{45}Y_{15}Cu_{40}$ ($\Delta T = 35$ K),[89] $Mg_{49}Y_{15}Cu_{36}$ ($\Delta T = 42$ K),[90] $Ti_{50}Cu_{28}Ni_{15}Sn_7$ ($\Delta T = 55$ K),[91] and $Al_{75}Ni_{10}Ti_{10}Zr_5$ ($\Delta T = 49$ K),[92] generally do not result in fully amorphous compacts, but instead contain nanocrystalline regions within the bulk.

A final consideration is time of sintering.[93] From the kinetics of phase transformations, minimizing time is always desired to avoid crystallization.[94] Indeed, a significant effort in defining appropriate manufacturing conditions is connected to the development of devitrification with respect to time and temperature. For example, **Figure 6** illustrates a time–temperature diagram with respect to the formation of crystalline regions, i.e., a time–temperature–crystallinity (TTC) diagram obtained from X-ray diffraction, in amorphous alloys of $Fe_{48}Mo_{14}Cr_{15}Y_2C_{15}B_6$ (Figure 6a) and $Fe_{49.7}Cr_{17.7}Mn_{1.9}Mo_{7.4}W_{1.6}B_{15.2}C_{3.8}Si_{2.4}$ (Figure 6b).[94] These diagrams can serve as a roadmap for determining changes in percent crystallinity with respect to time and temperature, whereas differential scanning calorimetry (DSC) can serve for more direct quantification of initial crystallinity, change of crystallinity, and crystallinity percentage as a function of temperature.[95] DSC can also be used to determine a variety of other thermodynamic properties, including heats of transformation, specific heat capacities,[96–98] and enthalpy–temperature–time (ETT) diagrams.[99]

Other techniques have also been used to determine phase stability diagrams. For example, Kim et al.[100] experimentally defined a complete time–temperature–transformation (TTT)

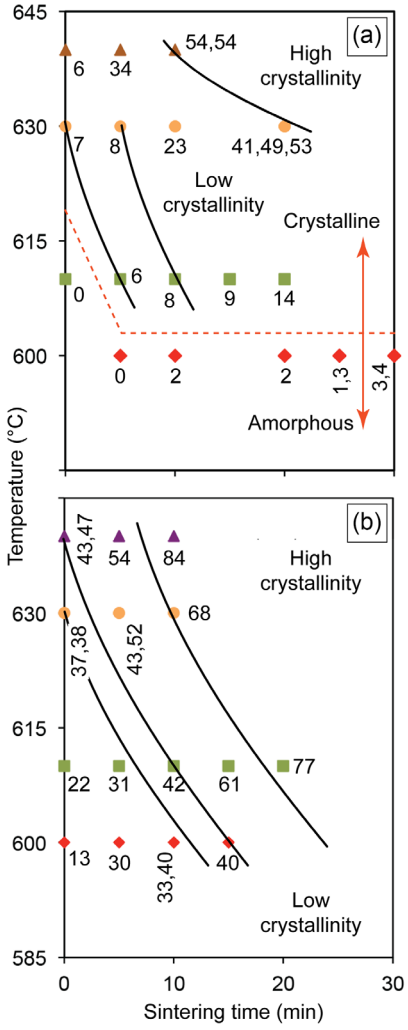

Figure 6. TTC diagram for a) $Fe_{48}Mo_{14}Cr_{15}Y_2C_{15}B_6$ and b) $Fe_{49.7}Cr_{17.7}Mn_{1.9}Mo_{7.4}W_{1.6}B_{15.2}C_{3.8}Si_{2.4}$. In these diagrams, the numbers under the data points describe the crystallite sizes in nanometers and the solid lines represent approximations to constant crystallite size. Reproduced with permission.[94] Copyright 2013, Elsevier.

diagram for the crystallization of a $Zr_{41.2}Ti_{13.8}Cu_{12.5}Ni_{10.0}Be_{22.5}$ alloy for the entire range of the undercooled liquid, from the melting point down to the glass transition temperature, using a high-temperature high-vacuum electrostatic levitation technique. **Figure 7**a summarizes all the measured times for the onset of crystallization at various isothermal temperatures. It shows the typical "C" shape, with the nose of the TTT curve at 51 s and 850 K. This nose is located at a significantly higher temperature than expected based on traditional theories of solidification, not surprising considering that the kinetic process of crystallization for these materials is highly complex, such that different phases form at different temperatures and times during solidification. For the case of $Fe_{48}Mo_{14}Cr_{15}Y_2C_{15}B_6$,[95] crystallization was explored using in situ high-temperature X-ray diffraction, resulting in the formation of Mo_3Fe_3O, Fe, and either Cr_2B, $Cr_{21.30}Fe_{1.70}C_6$, or $Fe_{23}B_2C_4$ (or mixtures of these three phases) at different points during the heating process (see **Figure 8**).

The TTT diagram for $Pd_{40}Cu_{30}Ni_{10}P_{20}$ (Figure 7b) was obtained using differential scanning calorimetry[101] and fit to a model based on steady-state nucleation rate and 3D growth of the crystals, resulting in

$$t = \left(\frac{3x}{\pi I_v(T)[u(T)]^3}\right)^{1/4} \quad (1)$$

where t represents the time to crystallize a detectable fraction x during isothermal annealing, T is the temperature, and $I_v(T)$ and $u(T)$ are given by

$$I_v = \frac{A_v}{\eta(T)} \exp\left(-\frac{16\pi\sigma^3}{3k_B T[\Delta g(T)]^2}\right) \quad (2)$$

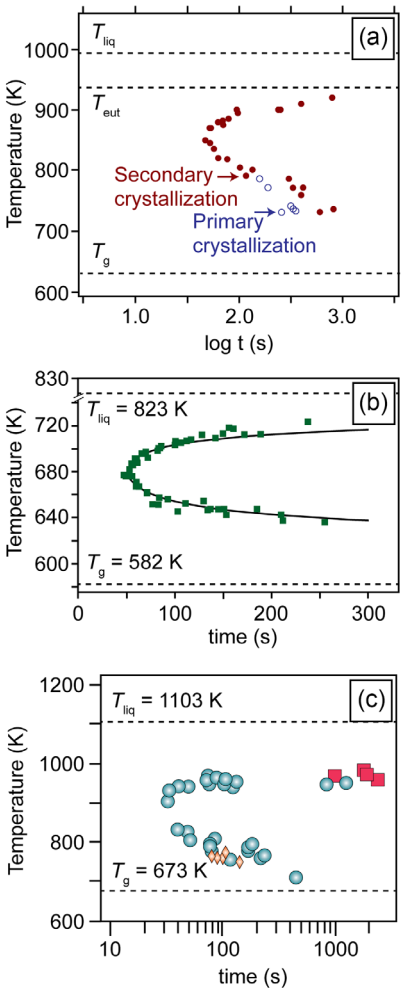

Figure 7. a) TTT diagram for $Zr_{41.2}Ti_{13.8}Cu_{12.5}Ni_{10.0}Be_{22.5}$ reflecting the onset of crystallization as a function of undercooling. Below 800 K two crystallization events were observed. The open circles represent the primary crystallization event and the closed circles represent the secondary crystallization event. Reproduced with permission.[100] Copyright 1996, AIP Publishing. b) TTT diagram of $Pd_{40}Cu_{30}Ni_{10}P_{20}$. Reproduced with permission.[101] Copyright 2000, AIP Publishing. c) TTT diagram of $Zr_{58.5}Nb_{2.8}Cu_{15.6}Ni_{12.8}Al_{10.3}$. Circles and squares denote data collected on cooling from the liquid state to an isothermal temperature. Diamonds depict data collected on heating from the amorphous state. Reproduced with permission.[103] Copyright 2001, AIP Publishing.

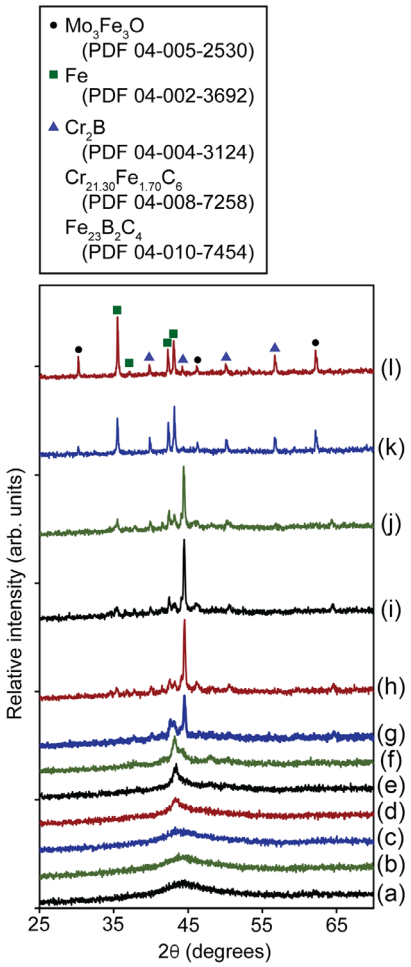

Figure 8. In situ X-ray diffraction patterns of $Fe_{49.7}Cr_{17.7}Mn_{1.9}Mo_{7.4}W_{1.6}B_{15.2}C_{3.8}Si_{2.4}$ powders in the temperature range from 823 to 1273 K. The temperatures at which each pattern was obtained are a) 823 K, b) 848 K, c) 873 K, d) 898 K, e) 923 K, f) 973 K, g) 1023 K, h) 1073 K, i) 1123 K, j) 1173 K, k) 1223 K, and l) 1273 K. Reproduced under the terms of the CC BY 4.0 license.[95] Copyright 2020 The Authors. Published by PLOS.

$$u = \frac{k_B T}{3\pi \ell^2 \eta(T)} \left[1 - \exp\left(-\frac{n\Delta g(T)}{k_B T}\right)\right] \quad (3)$$

Here, A_v is a constant of the order of 10^{32} Pa m^{-3} for homogeneous nucleation, η is the viscosity, Δg is the difference in Gibbs free energy (per unit volume), k_B is Boltzmann's constant, σ is the interfacial energy between the liquid and the nuclei, n is the atomic volume, and ℓ is the average atomic diameter. This model combines classical nucleation theory with a diffusion-controlled growth rate of the nuclei and is not applicable under all conditions. For example, materials such as $Zr_{41.2}Ti_{13.8}Cu_{12.5}Ni_{10}Be_{22.5}$ follow an Arrhenius-like effective diffusivity to describe crystallization time. The difference lies in the temperature dependency of viscosity,[102] with $Pd_{40}Cu_{30}Ni_{10}P_{20}$ having a larger viscosity at high temperatures, which slows down the kinetics of crystallization compared to $Zr_{41.2}Ti_{13.8}Cu_{12.5}Ni_{10}Be_{22.5}$. Further, the TTT diagram for alloy $Zr_{58.5}Nb_{2.8}Cu_{15.6}Ni_{12.8}Al_{10.3}$ is illustrated in Figure 7c[103] for comparison to Figure 7a. The two diagrams exhibit similarities in T_g and T_ℓ because both correspond to Zr-based alloys. The diagrams can be normalized with respect to T_g and nose time to intensify the similarities further, as illustrated in **Figure 9**.[104]

The TTC diagrams described earlier (Figure 6) were constructed from X-ray diffraction crystallite size results of samples obtained by spark plasma sintering (SPS).[105,106] This technique is now used for the consolidation of all families of materials, including ceramics and ceramic composites,[107–112] metal–ceramic composites,[113] and certainly metallic glasses.[114] Powders are placed inside a die and pressed while concurrently passing a very high current through the die and powders. The high current results in extremely fast heating rates through Joule heating and perhaps spark discharge[115] of the powders, which, when combined with quick cooling, can prevent devitrification of amorphous alloys. Typical pressures vary from ≈50 to 300 MPa and sintering times are usually no more than a few minutes. For example, $Fe_{65}Co_{10}Ga_5P_{12}C_4B_4$ powders of particle sizes lower than 125 μm were sintered using applied pressures of 80, 200, and 300 MPa and sintering temperatures of 723, 743, and 763 K,[116] resulting in specimens of varying densities. A sintering temperature of 723 K, which corresponds to the glass transition temperature of this alloy, resulted in amorphous sintered specimens. Higher temperatures resulted in some devitrification. Specimens manufactured at pressures of 80 and 200 MPa and temperature of 723 K contained some porosity, while the sample at a pressure of 300 MPa and temperature of 723 K had a density of 99.7% (i.e., fully dense). For a $Cu_{47}Ti_{33}Zr_{11}Ni_6Sn_2Si$ alloy[117] sintered at a pressure of 80 MPa and temperatures of 723–753 K, full density was only achieved at the higher sintering temperature of 753 K, causing some devitrification of the alloy, because the glass transition temperature in this material is 722 K. In fact, the sintering temperature is quite close to the crystallization temperature of 759 K. For the case of a Ni-based alloy ($Ni_{52.5}Nb_{10}Zr_{15}Ti_{15}Pt_{7.5}$),[118] a temperature of 773 K and an unusually high pressure of 600 MPa resulted in fully dense amorphous bulk specimens, whereas a temperature of 798 K caused devitrification. As the glass transition temperature of this material is 821 K, it is clear that devitrification can occur even when sintering at temperatures below the glass transition. A variety of reasons can explain this effect, including fluctuations in temperature inside the sintering die where internal temperatures can be significantly higher[105] than what is measured outside the die, usually with a pyrometer, especially if there is significant localized heating in the powders along contact surfaces. Thus, it is clear that temperature and pressure are important parameters during SPS. Lower temperatures are desirable for avoiding devitrification and higher pressures for achieving full density. An additional degree of freedom in controlling temperature/time/pressure involves the application of steps during heating. For example, a two-step process was used to sinter $Zr_{55}Cu_{30}Ni_5Al_{10}$,[119] resulting in samples that had higher densities than those obtained using a one-step sintering cycle.

As with sintering processes in other materials, powder particle size can have an influence on the capacity to achieve full density. For example, $Cu_{54}Ni_6Zr_{22}Ti_{18}$ powders of particle sizes between 33 and 45 μm achieved a density of 7.28 g cm^{-3}, whereas the alloy under the same sintering conditions and particle sizes of 91–150 μm only reached a density of 7.18 g cm^{-3}.[120] Appropriate size distributions, consisting of an optimized mixture of larger and smaller particles that are effectively mixed, are also necessary to achieve efficient packing.

Powders of $Ni_{59}Zr_{15}Ti_{13}Si_3Sn_2Nb_7Al$,[121] $Fe_{75}Nb_3Si_{13}B_9$,[122] $Cu_{46}Zr_{42}Al_7Y_5$,[123] $Zr_{55}Cu_{30}Al_{10}Ni_5$,[124] $Zr_{70}Cu_{24}Al_4Nb_2$,[125] $Ti_{45}Zr_{10}Cu_{31}Pd_{10}Sn_4$,[126] $Mg_{65}Cu_{25}Gd_{10}$,[127] $Hf_{55}Cu_{28}Ni_5Al_{12}$,[128] and $ZrCu_{39.85}Y_{2.37}Al_{1.8}$,[129] among many others, have also been prepared using the SPS technique with varying degrees of success, always optimizing for a temperature between the glass transition and crystallization temperatures, where the powders exhibit lower

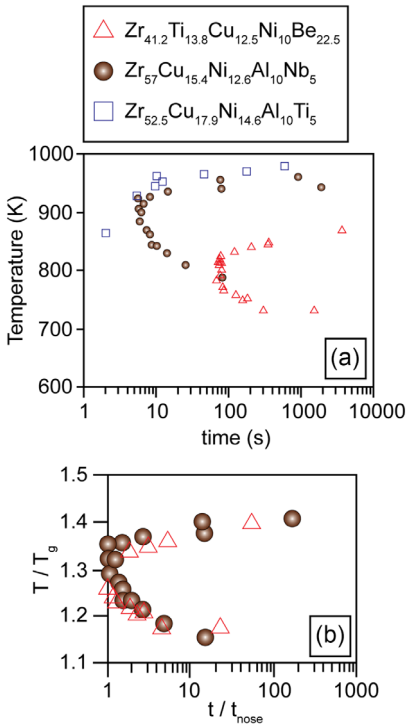

Figure 9. a) TTT curves for $Zr_{52.5}Cu_{17.9}Ni_{14.6}Al_{10}Ti_5$ (Vit105), $Zr_{57}Cu_{15.4}Ni_{12.6}Al_{10}Nb_5$ (Vit106), and $Zr_{41.2}Ti_{13.8}Cu_{12.5}Ni_{10}Be_{22.5}$ (Vit1). b) TTT curves for Vit1 and Vit106 that are normalized with respect to their glass transition temperatures and nose times. Reproduced with permission.[104] Copyright 2004, AIP Publishing.

viscosity. Indeed, the viscosity of the specimens is relevant at all temperatures and impacts sample contraction during the beginning stages of densification by[130]

$$\frac{\Delta L}{L_o} \cong \frac{3\gamma R T^2}{4DcQ\eta_o} \exp\left(-\frac{Q}{RT}\right) \tag{4}$$

where $\Delta L/L_o$ is the change in axial length of the specimen based on ram displacement, γ is the surface energy of the powders, R is the gas constant, T is the temperature, D is the average particle diameter, c is the heating rate, Q is the activation energy for viscous flow, and η_o is the pre-exponential constant in

$$\eta = \eta_o \exp\left(\frac{Q}{RT}\right) \tag{5}$$

Equation (4) and (5) assume that γ, η_o, and Q are temperature-independent, a reasonable approximation over small temperature intervals. The mechanisms of densification can also be defined from the point of view of friction between particles.[131] Some studies have also looked at the sintering behavior at temperatures below the glass transition temperature, resulting in samples of significant porosity[132] or that suffer from devitrification because of the need for longer sintering times to achieve higher densities.[133] However, under conditions of much higher pressures (i.e., 400 MPa), powders sintered at temperatures below the glass transition can result in 97–98% relative densities for $Fe_{48}Cr_{15}Mo_{14}C_{15}B_6Y_2$.[134]

A typical methodology to determine extent of devitrification after sintering is to examine the crystallization enthalpy of the samples by DSC. Even when sintered specimens are X-ray amorphous, initial relaxation of the alloy can occur during sintering, resulting in a reduction of the crystallization enthalpy. For example, the crystallization enthalpy of $Zr_{57}Cu_{20}Al_{10}Ni_8Ti_5$[135] reduces from a value of 61.9 J g^{-1} for the bulk powders to values as low as 23.7 J g^{-1} for a sample highly devitrified. Specimens that appear X-ray amorphous exhibit crystallization enthalpy values of 45.2 J g^{-1}, after sintering at a temperature of 663 K, a hold time of 10 min, and a powder particle size of 63–125 μm.

Other optimization parameters during SPS are the heating rate and hold time. For both parameters, the ideal scenario is to heat as fast as possible to the sintering temperature and hold for only a few minutes. Lower heating rates between 20 and 140 K min^{-1} do not seem to impact the final density significantly,[136] thus the use of higher heating rates is practiced more often to minimize time for the entire process. Typical hold times at the sintering temperature are 5 min or less,[137] because longer times will result in devitrification, especially at higher temperatures. A disadvantage of the process is the limitations on sample shapes. The technique is predominantly used to obtain disks of diameters between 1 and ≈5 cm (can be larger for systems that can achieve higher loads and currents) and a few millimeters in thickness.[138,139] Samples would then need to be machined to obtain other shapes.

2.2.3. Additive Manufacturing

A significant advance in the production of amorphous alloys is connected to the development and availability of 3D printing technologies, which can effectively circumvent size and geometry constraints that limit components produced by other techniques. Although considerable progress has been made in producing larger specimens by casting, there are definite limits that cannot be exceeded because of the need to overcome the critical cooling rate of the alloy through quenching. Spark plasma sintering is also limited in that it only produces flat cylindrical specimens of small sizes, although some attempts at producing some shape complexities are being explored.[140–142] Thus, there is increasing importance of 3D printing to fill this gap. As with all other manufacturing techniques for metallic glasses, the issue of devitrification is of critical importance and by necessity a main target of study in this field.[143,144] Focused reviews on this powerful family of techniques are available on the topics of 3D microfabrication,[145] laser powder bed fusion,[146,147] binder jetting,[148] selective laser melting,[149] and inkjet 3D printing.[150] For the interested reader, many general overviews are also available.[151–166]

In general, additive manufacturing involves the deposition of layers and the joining of these layers to form a 3D design, precisely why complex geometries are possible. There are many variations to 3D printing, with metal manufacturing currently based mostly on the powder bed fusion technique. Here, thin layers of powder are applied to a plate, after which a laser beam or an electron beam is used to fuse the powders at targeted locations. As each layer is finished, a new layer of powder is applied, until the desired component is complete. At each location where the beam is focused, a volume of only a few cubic millimeters or less is involved, which means that the heat can be applied and extracted quickly, enabling the formation of metastable materials, including metallic glasses. In laser beam systems, a flow of gas (usually inert nitrogen or argon) is passed over the powder bed to protect the materials from oxidation, whereas electron beam systems require a vacuum in the chamber to maintain focus of the beam. Comparisons between specimens produced by casting and selective laser melting have shown that alloys of $Zr_{59.3}Cu_{28.8}Nb_{1.5}Al_{10.4}$ prepared by the two techniques result in significant differences in fracture toughness values of 138.0 ± 13.1 and 28.7 ± 3.7 MPa m$^{1/2}$ for the cast and laser melted specimens, respectively, a result of the greater dissolved oxygen in the laser-processed material, which decreases atomic mobility and increases the activation energy required to initiate shear transformations necessary for improved material toughness.[167] Oxygen also modifies the path to crystallization, resulting in the formation of intermediate oxygen-rich metastable cubic phases that are not present in the specimens prepared by casting.[168]

Initial attempts at 3D printing of amorphous alloys focused on the manufacturing of simple shapes (shells, solid cubes, and coatings), such as those shown in **Figure 10**a.[169] Here, gas-atomized powders of $Fe_{58}Cr_{15}Mn_2B_{16}C_4Mo_2SiWZr$ (particle size: 10–110 μm) were deposited into a stainless steel substrate and spot-treated using a Nd:YAG laser operating at a maximum power of 650 W. The beam diameter at the focal point was <0.5 mm and the energy density varied from 2×10^4 to 1×10^5 W cm^{-2}. The process generally requires that the powder particles melt during laser heating and then resolidify. As crystallization must be avoided, the initial layers that are closest to the substrate undergo quenching and are predominantly amorphous. Unfortunately, as layers continue to be deposited, quenching is not as effective and subsequent layers undergo varying degrees of devitrification consisting of α-Fe, γ-Fe,

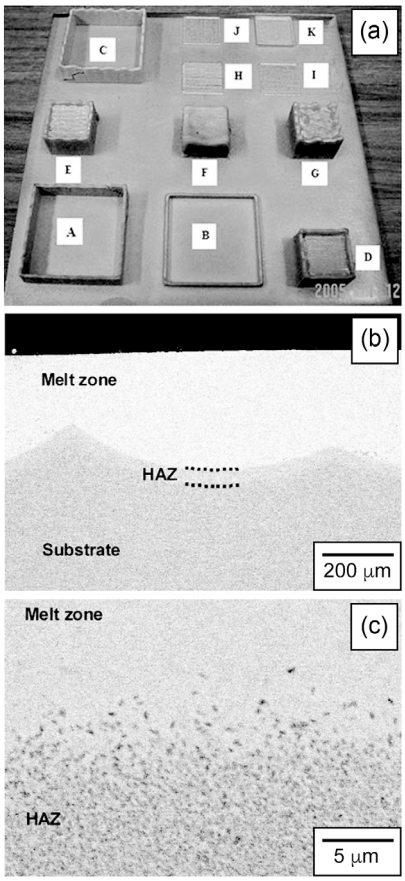

Figure 10. a) Initial simple shapes (shells, solid cubes, and coatings) produced by 3D printing. Reproduced under the terms of the CC BY-NC 2.0 license.[169] Copyright 2009, The Authors. Published by Springer Nature. b, c) Cross-sectional backscattered scanning electron micrographs of laser-deposited layers on crystalline substrates processed at a laser power of 150 W and travel speed of 21.2 mm s^{-1}. A continuous melt zone is observed in (b) above a thin crystalline HAZ and the substrate. The interface between the melt zone and nanocrystalline HAZ is shown at higher magnification in (c). Reproduced with permission.[187] Copyright 2010, Springer Nature.

tetragonal Fe_2B, cubic $Cr_{23}C_6$, and some unidentified phases. The process itself is defined by a complex thermal history connected to the numerous reheating cycles as the laser is scanned across each layer. In fact, this issue continues to be an area of primary concern, with numerous studies describing computational and analytical models that describe heat distributions, nucleation processes, and other relevant considerations.[170–181] The two parameters that predominantly control both temperature and cooling rate within a specified region of each layer are the laser output power and travel speed

$$E_\ell = \frac{P}{v \cdot d} \tag{6}$$

where E_ℓ is the energy intensity of the laser beam, P is laser output power in Watts, v is the laser travel speed in mm s^{-1}, and d is the laser beam spot diameter in mm. This equation ignores a variety of complexities in the process, including gas flow during deposition; nonetheless, it is useful as a first approximation. For a fixed laser power, the energy intensity on the powder will increase when d and v are decreased. As the energy intensity is increased, so will the size of the heat-affected zone (HAZ), which will not just affect the top layer, but lower layers as well. An analysis of scan speed and laser power with respect to density (**Table 1**) shows that higher laser powers and scan speeds will increase density, achieving values of 99.7% in $Fe_{68.3}C_{6.9}Si_{2.5}B_{6.7}P_{8.7}Cr_{2.3}Mo_{2.5}Al_{2.1}$ alloys.[182] Contour maps (**Figure 11**) of laser power and scan speed can also be used to explore variations in density.[183] From the point of view of characterization, microcomputed tomography has been effectively used to determine pore distributions within manufactured specimens.[184,185]

Clearly, laser power and scan speed, which define the temperature that each layer achieves, can be optimized to achieve higher densities while possibly adversely affecting the capacity of the material to maintain its glassy structure.[186] Figure 10b,c shows the formation of a typical HAZ between the substrate and the first layer of a $Zr_{58.5}Cu_{15.6}Ni_{12.8}Al_{10.3}Nb_{2.8}$ alloy,[187] which still devitrifies in spite of its excellent stability and glass-forming ability (GFA).[188] One solution is to delay the time of deposition of the next layer, so that the newly formed layer has time to cool. For the case of an alloy of approximate $Fe_{35}Cr_{25}Mo_{15}W_{10}C_3Mn_5Si_2B_5$ composition, a 5 s delay between layers aided in preventing devitrification.[189] In managing all these variables, it is noted that there will always be temperature differences from one layer to the next, with lower layers perhaps reaching all the way to room

Table 1. Relative density map of $Fe_{68.3}C_{6.9}Si_{2.5}B_{6.7}P_{8.7}Cr_{2.3}Mo_{2.5}Al_{2.1}$ samples as a function of laser power (P) and scan speed (v).[182]

Scan speed, v [mm s^{-1}]				
Laser power, P [W]	4500	3500	2500	1500
280	No consolidation of powders		70.1%	81.6%
300			72.2%	99.1%
320			77.6%	99.3%
340			83.7%	99.7%

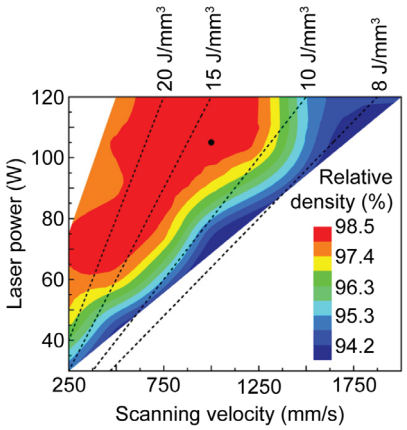

Figure 11. Contour map of laser power and scan speed describing variations in density for a $Zr_{52.4}Cu_{18}Ni_{14.6}Al_{10}Ti_5$ alloy. Reproduced with permission.[183] Copyright 2017, Elsevier.

temperature (or the temperature of the substrate) while the top layer maintains a temperature close to melting temperature, albeit for only a short period of time. These temperature differentials inevitably cause stresses between layers, which can be controlled by rescanning to maintain a higher temperature within the supercooled liquid region of the alloy. For an alloy of $Al_{85}Ni_5Y_6Co_2Fe_2$, the rescanning process resulted in the formation of significant amounts of aluminum and other intermetallic crystalline regions,[190] thus rescanning can be detrimental to maintaining the amorphous structure. Scanning strategies have also been explored to improve the chemical homogeneity within the melt region, resulting in significant improvement of the amorphous character of $Zr_{52.5}Ti_5Cu_{17.9}Ni_{14.6}Al_{10}$ specimens.[191] Results show that multiple scans help in promoting favorable mixing of the constituent elements within the melt, thus preventing inhomogeneous distribution of the elements that may become the source of nuclei and eventual crystallization. Also, two-step melting consisting of preliminary laser melting, followed by short-pulse amorphization, has been introduced to maximize the fraction of the glass phase.[192]

Geometric parameters during deposition also require optimization. In particular, the hatch spacing (i.e., the distance between one full deposition line and the next) and the orientation of scanning can be tuned to reduce porosity in the final samples. For an $AlSi_{10}Mg$ alloy,[193] when hatch spacing was increased beyond 150 μm, gaps were observed between adjacent scan lines. By also controlling the orientation of scanning—longitudinal and lateral—specimens of densities greater than 99% were achieved. Unfortunately, the samples were devitrified and, thus, did not achieve the objective of an amorphous specimen. Indeed, hatch spacing is recognized as important for devitrification; thus, it is sometimes taken into consideration in Equation (6), resulting in a modified equation of the following form

$$E_\ell = \frac{P_{\text{eff}}}{v\,h\,t} \tag{7}$$

where E_ℓ is the energy density or energy input from the laser in J mm^{-3}, P_{eff} is the effective laser power in Watts, v is the laser scan speed in mm s^{-1}, h is the hatch distance in mm, and t is the layer thickness of the powder bed in mm. Even here, the equation is an approximation that ignores hatch style, laser spot size, and material properties such as thermal conductivity and reflectivity.[194] As a summary and for guidance, a full list of processing parameters is illustrated in **Figure 12**.[193] Particle size considerations have not been discussed in detail in this review, as they have been examined in other reviews.[143,195,196] Generally, smaller particles are of benefit for 3D printing as they spread more readily and can melt more easily compared to much larger particles.

2.2.4. Spraying Techniques/Coatings

Coatings can provide improved properties to components that may not meet engineering requirements and are, thus, extremely important for broadening options in a variety of applications. For the case of metallic glasses in the form of coatings, corrosion and wear protection is of particular interest and has been thoroughly explored in the literature.[197–203] There are two principal techniques for manufacturing amorphous metal coatings, laser-based

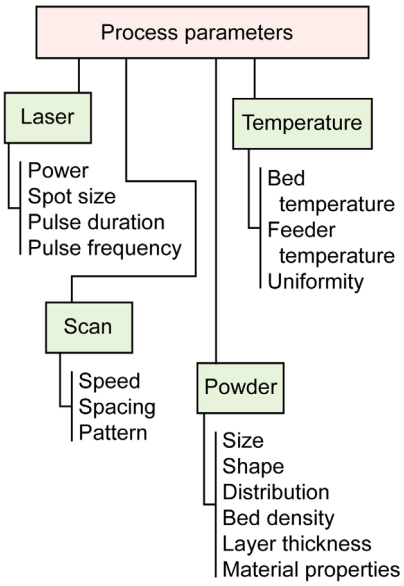

Figure 12. Controlling parameters in selective laser melting. Reproduced under the terms of the CC BY 3.0 license.[193] Copyright 2014, The Authors. Published by Elsevier.

processes and thermal spraying. Laser-based techniques have similar characteristics and merits to those used during 3D printing[204] and, indeed, the manufacturing of coatings preceded 3D printing and informed the field. In the same way as 3D printing functions, the fabrication of a coating initiates by depositing a powder layer onto a substrate and then scanning a laser beam across the powder. Issues associated with the heat-affected zone that melts, cools, and then reheats are extremely relevant and devitrification of the coating can easily occur if the heat input into the system is not carefully optimized. Laser power, scan time, and type of substrate that can transport heat away from the coating are just as relevant here as they are for 3D printing.[205]

Thermal spray techniques are well known and a variety of topical reviews are available that describe the relevant variables and conditions for optimization,[206–218] including some on amorphous metals.[205,219,219,220] It is not surprising that manufacturing of amorphous metal coatings can easily suffer from devitrification, as is the case with the production of bulk samples. Typical parameters for achieving positive outcomes are listed in **Table 2** for the case of Fe-based coatings,[220] which are generalizable to other alloys. In its most general description, the process consists of heating feedstock particles to a molten or semimolten state and spraying into a substrate. As the droplets impinge on the substrate, they flatten and solidify, forming stacked layers. Early activities on the production of coatings are now several decades old, consisting mostly of examples of partially devitrified coatings.[221–223] As understanding of the technique improved, amorphous coatings were then successfully manufactured. For the case of fully amorphous $Ni_{57}Ti_{18}Zr_{20}Si_2Sn_3$ and $Cu_{54}Ni_6Zr_{22}Ti_{18}$,[224] coatings were achieved at a powder temperature close to room temperature, possible because of the application of a high kinetic energy to the impacting particles (apparatus set travel speed = 0.01 m s^{-1}; powder feed rate = 36 g min^{-1}; transport gas = helium; gas

Table 2. Thermal spray methods for the preparation of Fe-based amorphous coatings.[220]

Parameter	Arc spray	Plasma spray	High-velocity oxygen fuel spray
Feedstock materials	Cored wires	Amorphous powders	Amorphous powders
Jet temperature [K]	>25 000	>10 000	5500
Particle temperature [K]	>3800	>3800	3300
Particle velocity [m s^{-1}]	50–100	200–800	200–1000
Cooling rates [K s^{-1}]	$\approx 10^5$	$\approx 10^6$–10^7	$\approx 10^4$
Coating hardness [HRC]	40	40	45
Coating thickness [mm]	0.4–0.5	0.05–0.5	0.1–1.2
Porosity [%]	3–10	2–5	<2
Density range [%]	80–95	90–95	>95
Oxygen content [%]	0.5–3	0.5–1	<0.2
Bonding form	Micrometallurgical	Mechanical	Semimetallurgical
Bond strength [MPa]	10–40	<68	>68
Cost	Low	High	Higher

temperature = 550 °C; particle size of powders = ≈45 μm). The coatings appeared to contain some porosity after corrosion testing over a period of 9 days. As micrographs before corrosion testing were not presented, it is not possible to ascertain the extent of porosity in the as-prepared coatings. For the case of a $Ni_{53}Nb_{20}Ti_{10}Zr_8Co_6Cu_3$ alloy,[39] a helium gas temperature of 570 K was optimized for manufacturing coatings with porosity that, unfortunately, was not quantified (approximating from a scanning electron micrograph, there is about ≈5% porosity in coatings of 400 μm thickness). Generally, lowering the temperature during the spraying process can result in fully amorphous coatings at the detriment of density because lower temperatures will prevent deformation of the powders to form splats for full coverage. Recalling the TTT diagrams in Figure 7, which defines the behavior of the powders during densification, at temperatures significantly below the glass transition temperature, the powders do not deform significantly and are not able to bond to the substrate, whereas in the supercooled liquid region, significant deformation is expected. Here again, the particle size of the starting powders is relevant. Wu et al.[225] found that small particle size affects the acceleration of the particles as they are being deposited. Smaller particles of 10 μm sizes achieve higher velocities of 939 m s^{-1} during flight, affecting the energy of deposition. These smaller particles can also be fully molten during flight if the travel distance is not excessive. For longer flight distances (and times), the particles can begin to solidify before reaching the deposition substrate because of their smaller thermal inertia. Larger particles between 40 and 60 μm cannot achieve the velocities seen with the smaller particles and may also not reach the melting temperature. Thus, they are not ideal for achieving coatings that are highly dense. Generally, higher particle velocities result in improved splat formation, as the particles will impact at a higher kinetic energy. This must be combined with appropriate melting of the particles because lower porosity is only achieved if the particles are molten. However, if the temperature is too high and the coating is prepared in air, then higher temperatures result in detrimental oxidation.[226]

In addition to laser-based and pyrolysis techniques, there is the opportunity to produce coatings using electrodeposition processes. Electrodeposition is less common and makes use of salt precursors, instead of metal elements. The process is controlled by current density because it greatly influences both the rate of crystal nuclei formation and the rate of crystal growth. For higher current densities (i.e., higher than the rate of nuclei formation), deposition will occur without formation of nuclei and eventual growth of crystals. Thus, higher current densities can result in amorphous coatings. For example, the preparation of $Ni_{100-x}P_x$ ($x = 0$, 5, 10, 15, and 25 at%) amorphous coatings[227] made use of an electrolyte of phosphorous acid (H_3PO_3), nickel sulfate ($NiSO_4{\bullet}6H_2O$), nickel chloride ($NiCl_2{\bullet}6H_2O$), boric acid (H_3BO_3), and sodium dodecyl sulfate ($NaCl_2H_{25}SO_4$), a cathode of copper, and an anode of nickel. The electrodeposition process was controlled by varying the peak current densities, using 20 A dm^{-2} for $Ni_{95}P_5$, 17 A dm^{-2} for $Ni_{90}P_{10}$, 12 A dm^{-2} for $Ni_{85}P_{15}$, and 5 A dm^{-2} for $Ni_{75}P_{25}$. Not all compositions resulted in amorphous coatings. Loss of amorphous character was evident as the current density was decreased, corresponding to increases in the amount of phosphorus in the systems studied, with composition $Ni_{75}P_{25}$ exhibiting very clear diffraction peaks in its X-ray diffraction pattern. Beyond control of current density, bath temperature (≈40 °C) and pH must be tuned to avoid compositional variations in the coatings, especially for those that take several hours of deposition. For these $Ni_{100-x}P_x$ compositions, deposition times were varied from 0.5 to 4 h depending on the desired thickness of the coatings, which was several micrometers to >2.5 mm. Thus, the process can be significantly protracted compared to thermal spray techniques. Long processing times can be balanced by using moderate temperatures, which can be an advantage from the point of view of energy efficiency. Unfortunately, highly complex multicomponent coatings are likely not achievable by this technique, as control over the simultaneous deposition of many types of elements is difficult. Despite this limitation, the electrodeposition process offers flexibility in the shape of the substrate compared to other techniques.

2.3. Postprocessing

Engineering components may require machining into specific shapes, to modify the size of a specimen beyond the limits obtained from the manufacturing techniques discussed previously and achieve high dimensional accuracy, or to provide finished surfaces with minimal surface roughness. Generally, cutting and polishing are implemented to modify dimensions and provide smoother surfaces. Welding can also be used to join components into larger specimens.

2.3.1. Machining and Cutting Techniques

Machining techniques for metallic glass components vary depending on size (i.e., micrometer to macrometer scales).[22,228] Typical cutting processes to reduce dimensions in macroscopic specimens have specific challenges associated with the low thermal conductivity of most metallic glasses, which can result in very significant and rapid heating of the part, to the point that surface crystallization and oxidation (if cutting is in air) may occur. As an example, significant thermal radiation was seen during lathe turning of a $Zr_{41.2}Ti_{13.8}Cu_{12.5}Ni_{10.0}Be_{22.5}$ amorphous alloy,[229] a sign of the higher temperatures of the sample resulting in surface oxidation. As the cutting speed was increased from values of 0.38 to 1.52 m s^{-1}, light emission also increased, and oxidation became more problematic. Removal of heat from the system is one mechanism that allows temperatures to remain lower. With samples that have lower conductivity, an option is to select cutting tools made of materials of higher thermal conductivities such as WC–Co[230] or diamond.[231] Bakkal et al.[229] showed that a tool with thermal conductivity of 560 W m^{-1} K minimized light emission and oxidation during cutting, compared to a tool with thermal conductivity of 72 W m^{-1} K. The removal of heat from the surface can also prevent welding between the cutting piece and the tool, an issue that was also described by Bakkal et al.,[229] and prevent other damage to the tool in general.[232] On a similar alloy of composition $Zr_{52.5}Ti_5Cu_{17.9}Ni_{14.6}Al_{10}$,[233,234] results show that above a threshold cutting speed, the low thermal conductivity of the alloy leads to chip oxidation of the zirconium (forming ZrO_2) reaching temperatures of ≈2700 K, causing crystallization and significant viscous flow. Nanocrystalline phases of ≈10 nm in size were also formed of compositions Zr_2Cu, $ZrAl_2$, and Zr_2Ni.[235]

The feed rate of the specimen is another important consideration to avoid devitrification. For $Zr_{52.5}Ti_5Cu_{17.9}Ni_{14.6}Al_{10}$ rods cut in dry conditions without coolant,[236] a higher feed rate of 4000 mm min^{-1} resulted in specimens that did not crystallize, even though the temperature that was reached during cutting was greater than the glass transition temperature. This effect can be attributed to the lower contact time between the specimen and the cutting tool. Comparatively, feed rates of 1000 and 2000 mm min^{-1} resulted in cut specimens that were devitrified because of the additional time allowed for the devitrification transformation. Typically, removal of surface material in amorphous alloys results in continuous lamellar chips[237,238] containing shear bands (see **Figure 13**). Modeling of the process shows that increasing cutting speed and depth of cut will result in these lamellar chips. However, if the amorphous alloy has a higher initial free volume and larger Poisson's ratio (or shear modulus), it will respond by forming decreasing volumes of lamellar chips. These considerations are necessary when choosing the cutting material. Softer alloys that form lamellar chips can be cut using steel tools, whereas harder alloys that do not form lamellar chips require tools such as diamond.

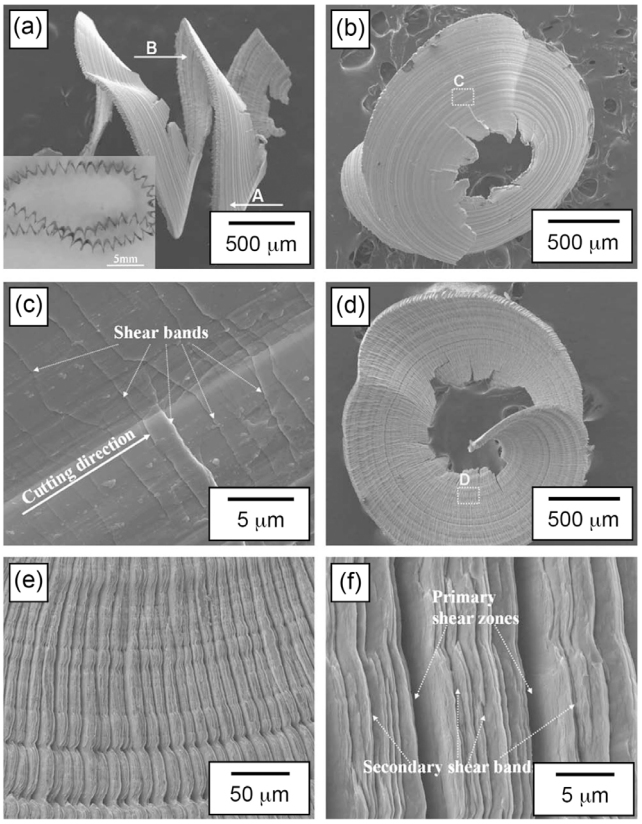

Figure 13. Chip morphology of a Zr-based alloy. a) Macroscopic view of a typical continuous twist chip. b) Tool contact surface of chip marked by "A" in (a). c) Details corresponding to area "C" in (b). d) Free surface of chip marked by "B" in (a). e,f) Lamellar structures at different magnifications in area "D" in (d). Reproduced with permission.[237] Copyright 2009, Elsevier.

Beyond cutting techniques for larger specimens, machining of micrometer specimens requires more refined techniques such as laser pulsing,[20] which may be in the femtosecond, picosecond, nanosecond, or microsecond time scales. Longer times may result in crystallization, but are more effective in material removal; thus, there is a compromise between longer laser pulse times, which result in larger energy transfers to the specimen,[239] and shorter pulse times that are effective at impeding crystallization. A single laser pulse results in a crater that usually exhibits signs of substrate melting, as illustrated in **Figure 14**a,b for $Ni_{78}B_{14}Si_8$,[240] although the deposited material can also be attributed to sublimation and redeposition of the vapor on t he substrate. If the laser beam is scanned across an entire substrate surface, removal of a substrate layer can be achieved. Repeated scanning can then be effective for removing significant surface material. The laser can also be used for drilling holes

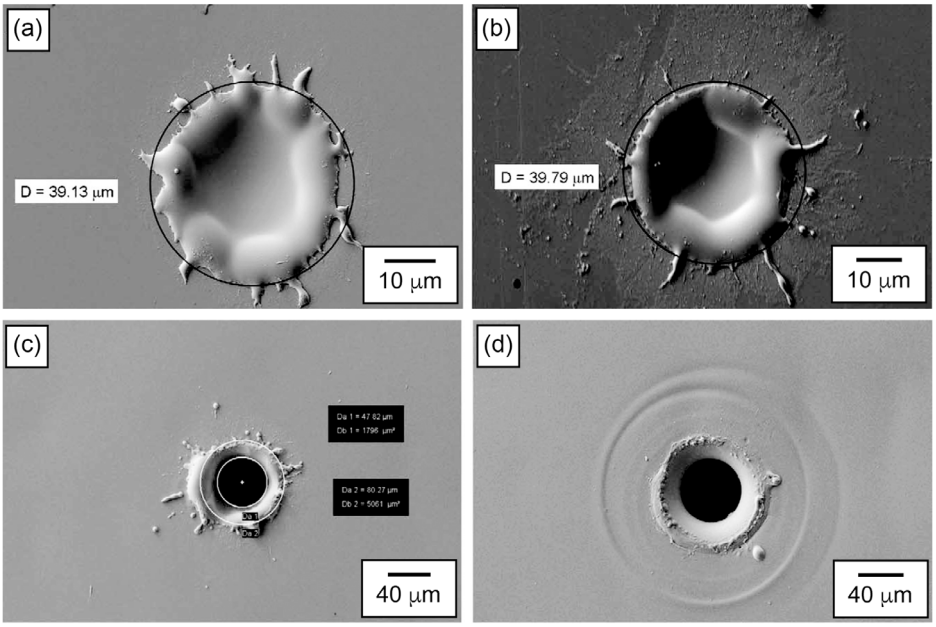

Figure 14. Scanning electron micrographs of single pulse craters produced by μs laser ablation of Ni-based amorphous alloys using average laser power of a) 3 W and b) 3.1 W. c,d) Scanning electron micrographs of holes machined by μs laser using average laser power of (c) 3.3 W and (d) 4.7 W. Reproduced with permission.[240] Copyright 2009, Elsevier.

(Figure 14c,d), which usually requires higher laser power and, thus, significantly higher heat loads on the substrate. This may result in devitrification if the temperatures reached by the substrate exceed the glass transition temperature for extended periods. The selection of laser type also has an impact on crater size and heat to the system[241] because the irradiated region (i.e., the spot size) is directly proportional to the wavelength of the photons

$$D_o = 1.22 \times \left(\frac{\lambda \times F}{n \times W_d}\right) \times M^2 \quad (8)$$

where λ is the laser wavelength, F is the focal length, n is the refractive index, W_d is the diameter of the incident laser, and M^2 is the laser quality factor. Under nonoptimized conditions, laser surface treatment can result in thermal mismatch cracking that leads to extrusion of the alloy out of the cracks. A specific example can be found for the case of $Zr_{41.2}Ti_{13.8}Cu_{12.5}Ni_{10}Be_{22.5}$ rods,[242] which were surface irradiated using a Nd:YAG laser in a nitrogen gas environment. The presence of nitrogen resulted in the crystallization of ZrN on the surface, causing thermal mismatch and then cracking. Similarly, one can find the formation of networked erbium oxides in $Fe_{52}Cr_{13}Mo_{12}C_{15}B_6Er_{22}$.[243]

An additional option for machining small components, micro-electrical discharge machining (micro-EDM), can be adapted from conventional EDM.[244–253] In this case, the material removal process occurs because of the combined melting and vaporization of the specimen and the electrode, due to the intense heat generated during electrical discharging between them. For micro-EDM to be effective, the specimens must be electrically conductive, making the technique amenable to the cutting of amorphous metals. Micrographs of $Zr_{57}Nb_5Cu_{15.4}Ni_{12.6}Al_{10}$[254] in **Figure 15** illustrate

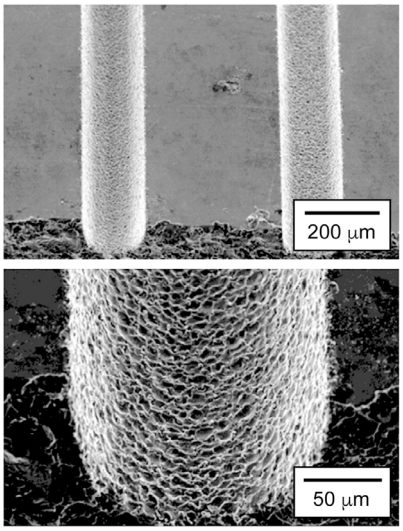

Figure 15. Micro-EDM grooves produced using an input energy of 13.4 μJ. Reproduced with permission.[254] Copyright 2009, Taylor & Francis.

the typical cratered topography of the process (input energy: 13.4 μJ). Smaller crater sizes (i.e., smoother surfaces) are achieved when using lower discharge energies. Quantitatively, decreasing the input energy from 13.4 to 0.9 μJ results in a 43–51% reduction in surface roughness and a 63% reduction in burr width due to the generation of smaller craters and smaller amounts of molten material. Decreasing input energy, however, results in increasing machining time for equal material removal, which may be economically undesirable. The application of EDM for the case of

$Zr_{38.5}Ti_{16.5}Cu_{15.25}Ni_{9.75}Be_{20}$[255] showed that surface roughness (R_a) could be empirically correlated to the discharge current (I_p) and pulse duration (τ_p) through

$$R_a = \beta(I_p \times \tau_p)^{\alpha} \quad (9)$$

where β and α are fitting parameters to experimental data. Clearly, lower discharge current and shorter pulse duration will result in a smoother surface.

A final parameter to consider is the electrolyte in which the specimen and electrode may be immersed. Many electrolytes cause significant oxidation of amorphous alloys, as seen during the electrochemical machining of $Fe_{65.5}Cr_4Mo_4Ga_4P_{12}C_5B_{5.5}$ in aqueous solutions of $NaNO_3$, NaOH, and H_2SO_4, all three of which appeared not to be suitable as electrolytes,[256] or in $Zr_{57}Ni_{20}Al_{15}Cu_{5.5}Nb_{2.5}$ in aqueous solutions of $NaNO_3$.[257] There can be optimizations to the electrochemical machining process which can reduce or eliminate oxidation, evidenced during the machining of $Fe_{65.5}Cr_4Mo_4Ga_4P_{12}C_5B_{5.5}$ on an aqueous electrolyte of 0.1 M H_2SO_4 with up to 0.1 M $Fe_2(SO_4)_3$.[258] Here, the application of very short voltage pulses results in a dissolution process of oxide layers that may be forming during the cutting process. Micromachining of $Zr_{59}Ti_3Cu_{20}Al_{10}Ni_8$ is also possible using a methanolic $HClO_4$ solution.[259] Another option is to use nonaqueous electrolytes, as in the EDM of $Zr_{41.2}Ti_{13.8}Cu_{12.5}Ni_{10}Be_{22.5}B$ using EDM oil (CASTY-LUBE EDS).[260] When using oil, the sparking can result in breakdown of the organic into hydrogen, carbon, and other by-products, which is environmentally problematic, can deposit and contaminate the cut surfaces, and may also induce crystallization that results in surface ZrC. Replacement of petroleum-based electrolytes with biofuels such as canola and sunflower biodiesel has been attempted to realize more environmentally friendly EDM.[261] For Ni-based alloys such as $Ni_{72}Cr_{19}Si_7B_2$, the use of an aqueous $NaNO_3$ electrolyte results in poor slit quality and insoluble electrolysis products, whereas an aqueous 0.1M $H_2SO_4 + 1$ M H_2O_2 electrolyte results in smooth and cleaner surfaces, although there are still isolated islands and surface pits because of the variation in dissolution rates of the surface elements.[262] A 0.1 M HCl electrolyte can be also optimized to obtain a variety of structures of high fidelity;[263] nonetheless, H_2SO_4 is still better at producing more uniform surfaces.[264]

Another highly refined process for machining surfaces and microcomponents makes use of a focused ion beam (FIB). The technique is now well studied and effective in producing surface features in a variety of substrates.[265–269] A typical FIB uses gallium ions that erode the surface in highly intricate patterns. A variety of examples are shown in **Figure 16** for a $Zr_{55}Al_{10}Cu_{30}Ni_5$ amorphous alloy.[270] Here, as in any other cutting process, surface finish is important, and some studies have looked at the polishing of amorphous alloys by a variety of techniques such as abrasive jet polishing.[271] Details of grinding and polishing techniques can be explored in a variety of reviews.[272–280] Ultimately, achieving the manufacturing of components that do not require any machining is a goal in the form of new techniques such as thermoplastic forming of additively manufactured alloys.[281]

2.3.2. Welding

Laser welding,[282–287] friction welding,[288–293] electron beam welding,[294] and other variations are methods used to weld bulk metallic glasses to overcome size and geometry limitations of raw part manufacturing. During welding, maintaining the amorphous character at the weld bead is crucial to the success of the technique, and a variety of articles, from early[295] to later reports,[296–302] address this in depth. Techniques that produce a melt, such as laser welding and electron beam welding, can be successfully implemented only if the metallic glass has a high GFA. Otherwise, crystallization will occur upon solidification of the molten weld bead. In techniques where there is no molten phase, the welding process requires significant viscous flow between the components being joined.

A variety of parameters can be applied to improve the weldability of amorphous alloys. Composition is one such variable.

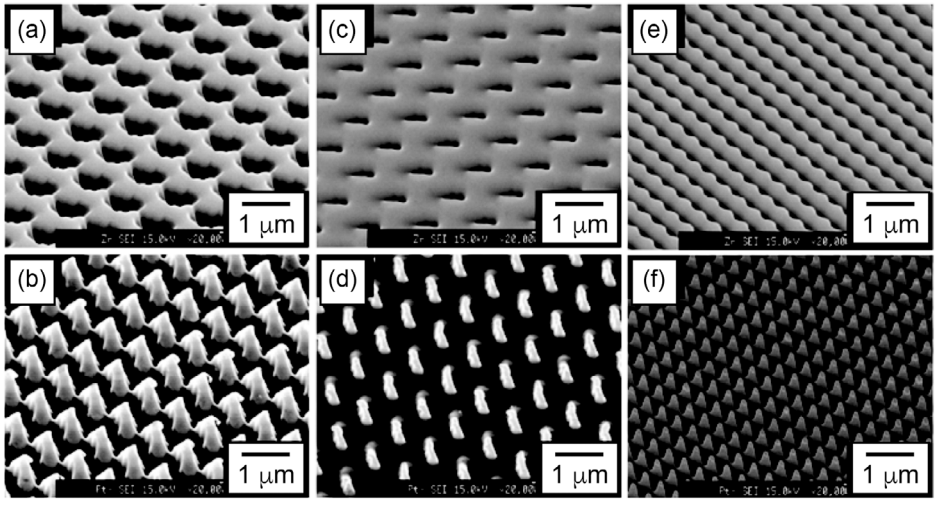

Figure 16. a,c,e) correspond to scanning electron micrographs of FIB machined die surfaces of a Zr-based metallic glass. b) Corresponds to a die-forged periodically nanostructured surface of a Pt-based metallic glass prepared using the die shown in (a). d) Corresponds to a surface prepared using die (c). f) Corresponds to a surface prepared using die (e). Reproduced with permission.[270] Copyright 2007, Trans Tech Publications Ltd.

For example, the addition of 0.02 at% scandium to $Zr_{55}Cu_{30}Ni_5Al_{10}$ minimizes the formation of Zr_2Ni and $Zr_2(Cu,Al)$ compounds[303] because of the increase in T_x of the $(Zr_{55}Cu_{30}Ni_5Al_{10})_{99.98}Sc_{0.02}$ alloy, which provides a higher resistance to devitrification. The effect is enhanced further if the welding process makes use of liquid nitrogen for accelerated cooling, freezing the amorphous character of the weld zone. Beyond composition, modification of experimental parameters can be exemplified by adjustments to laser pulse energy and pulse width during laser welding,[302] both of which cause devitrification when increased. Additional details on welding techniques are described by Kawamura.[304]

2.4. Challenges and Future Directions

As with many other materials classes, future directions and challenges in the processing of amorphous alloys are related to the need to design multifunctionality in these materials, for example, designing both higher strength and higher toughness, properties that are generally mutually exclusive. Examples of composites consisting of amorphous metal matrix and nanocrystalline dispersed phases were discussed earlier. These kind of materials can result in combined properties that may not be achievable from the individual components. Mixed amorphous metal composites (i.e., composites made of two or more types of alloys) may also provide options for properties control. Flexible processing techniques with a variety of controlling parameters that can quickly consolidate powders into larger bulk specimens are desirable to make these more complex composites in larger sizes. On the other hand, the manufacturing of components of a great variety of sizes and shapes requires continued advances and opportunities in 3D printing, which is currently the only option for making complex shapes. It is also the technique that can reduce wasted material since components are made to almost the shape in which they will be used.

3. Machine Learning Design Approaches

3.1. Preface

The computational design of amorphous alloys takes a variety of forms, including atomistic[305–312] and molecular dynamics approaches,[313–318] as well as newer artificial intelligence (AI)/machine learning (ML) techniques.[319–325] In the latter approaches, somewhat limited datasets for implementation are available, although there have been continuous improvements in the availability of data. Nonetheless, there are enormous uncharted areas of composition space in which metallic glasses with intriguing properties might be discovered, with some estimates exceeding 3 million.[326] Indeed, AI techniques are now being used in a wide variety of fields (i.e., multimedia,[327] among others) because of the increased availability of robust platforms for AI algorithm development, including TensorFlow,[328] Caffe,[329] and Keras.[330] Thus, the development and use of AI in materials science are increasing in importance and demonstrate great promise,[331–341] especially when connecting theory and experimentation.

On the experimental side, the GFA of an amorphous alloy represents the capacity of a material to maintain a glassy state upon quenching and is usually judged using parameters such as the critical casting diameter, the critical cooling rate, or the reduced glass transition temperature.[342] It represents a critical characteristic of amorphous alloys that is regulated by the chemical composition of the material. Consequently, understanding the relationship between GFA and composition is critical to the design and discovery of novel amorphous alloys. However, as stated earlier, the composition space is vast, resulting in challenges to explore the many opportunities available. To mitigate this problem, a variety of empirical and physical models have been proposed based on topology, thermodynamics, atomic size mismatches, valence electron distributions, atomic number fractions, and near deep eutectic compositions, among others.[343] However, a comprehensive model or approach with as many variables as simultaneously possible remains highly desirable. In this sense, AI can play a very important role in modeling the GFA by simultaneously considering many variables that can better predict new compositions with desirable properties. From this, a general scheme that addresses the relevant steps to accelerate amorphous alloys design and discovery is presented in **Figure 17**.

3.2. Collecting and Validating Data

The quality and size of the datasets used for training an AI algorithm are critical and require careful identification, gathering, and possibly the creation of new data through ab initio and other computational techniques. In terms of data quality, two criteria are relevant: 1) the experimental technique used to manufacture the alloys; and 2) the range and values of the alloy attributes. Regarding the manufacturing of the alloys, some authors specify that AI training should be only with data from alloys produced by copper-mold casting, to avoid any possible impact from sample manufacturing techniques.[342] Regarding alloy attributes, some researchers propose excluding extreme values, such as a high GFA, because the model accuracy may be affected due to the limited number of samples of such extremes.[344] Other authors have chosen to use the maximum or mean value of an attribute if the composition appears more than once in the dataset.[333]

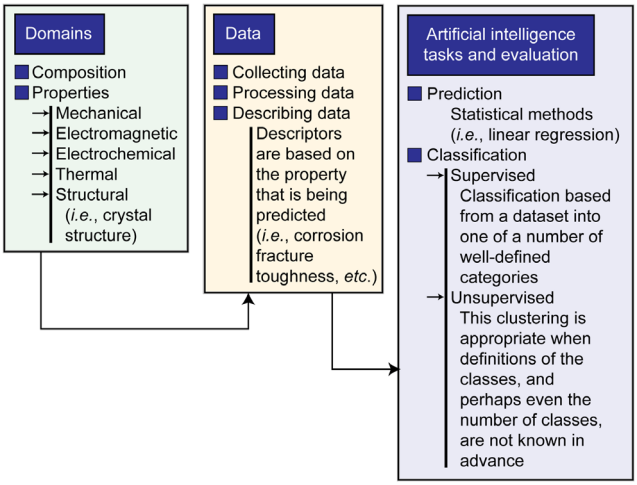

Figure 17. Stages during the development and optimization of an artificial intelligence/machine learning algorithm for amorphous metal alloy prediction and classification.

Discrepancies in attribute values can also exist for a variety of reasons, including human typing errors.[338] Thus, it is important to validate the data, especially when creating a dataset that comes from different sources. Examples of flaws include unrealistic or missing values, outliers, corrupt values, or poorly formatted values, including text-encoding errors, numbers stored in a nonnumeric format, and nonmatching data formats. **Table 3**[323,326,345] lists datasets of amorphous alloys that have taken some of these details into consideration. The "156 839" database associated with the Citrination site was created by Ward et al.[323] with the goal of training machine learning models to predict GFA as a function of composition. It contains 6656 alloys with details such as the GFA, critical casting diameter, supercooled liquid range, and glass transition temperature. Also, the information's structure is in the form of a Physical Information File (PIF) scheme, which is a more flexible syntax than a rigid file format such as a Crystallographic Information File (CIF). The "198 590" Citrination site[345] incorporates two datasets. One dataset contains 875 alloys with ten thermodynamic attributes, including the GFA. The second dataset contains 9894 compounds that are labeled as either metallic or nonmetallic glasses, as well as information for eight thermodynamic attributes. The last database[326] in Table 3 contains 177 metallic alloys presenting information on X-ray characterization and electrochemical characteristics for the study of glass formation in Ni–Ti–Al ternary alloys. The information contained in the database is structured and readable for use with some machine learning methods. There are, of course, other databases not specific to amorphous alloys that are very useful for applications in machine learning. For instance, the OQMD database[325] has information on the electronic properties of known crystalline solids. This database is based on thermodynamic and structural properties that have been calculated through density functional theory. The structure of the information is in Structured Query Language format (SQL) and in a query interface programmed in Python language. Among other contributions to materials modeling infrastructure is the Automatic Flow (AFLOW; http://aflowlib.org/) repository with information for high-throughput calculation of crystal structure properties of alloys, intermetallics, and inorganic compounds. The European Union's Novel Materials Discovery (NoMaD; https://nomad-lab.eu/) laboratory is also a repository for sharing materials science data. It is applicable to materials ranging from liquids, glasses, and highly ordered crystalline materials.

Evidently, the size of the dataset is another key concern. One of the challenges with amorphous alloys is the somewhat small size of the datasets available (≈6000 compositions in 60 years) compared to their crystalline counterparts (≈240 000 structures[331]). However, lately it has been demonstrated that with suitable information, AI models can work well even with small datasets.[346–348] Also, cloud environments have been created in recent years to maintain repositories and make them available to the research community,[349] which is undoubtedly of great help in moving the field forward.

Table 3. Currently available amorphous alloy databases.

Dataset	Reference
https://citrination.com/datasets/156839/	[323]
https://citrination.com/datasets/198590/	[345]
https://github.com/usnistgov/HTE-NiTiAl	[326]

3.3. Data Description

Data description, also known as featurization, fingerprinting, or feature engineering, involves the preparation of the input data in a format that the AI model can process satisfactorily. As a first step, the data must be converted into a set of variables to be engineered by the AI algorithm, typically as a sequence of scalar or vector variables for every dataset input. This step can involve the reconversion of current data (i.e., rescaling, normalization, binarization), such as physical properties, into a representation in regions or value spaces that allow a better description of the data. For instance, Lu et al.[321] used two features or data descriptions that have evidently different scales, the temperature that falls in the range of 800–>2000 K, and the average atomic radius difference (δ) that is less than 102. Therefore, it is essential to scale these data using a suitable algorithm. There are many algorithms to achieve such a goal, with most researchers utilizing min–max rescaling as data standardization.[324,347,350,351]

As a second step, high-quality data descriptors must be selected. At present, there are four main conventional points of view for devising a descriptor for AIs in amorphous alloys. The first concept is to manually create a new set of descriptors that rely on the specific physical and chemical properties of the experimental candidates. The second concept is to project the attributes of the experimental candidates into numerical vectors as descriptors by using related physical and mathematical theories based on statistics, probability, and other approaches. The third concept is a combination of the latter two, while in the fourth concept the descriptor is automatically created using convolutional deep learning. For example, Deng and Zhang[352] mathematically computed four descriptors that were not available experimentally, total electronegativity (based on Pauling electronegativities), atomic size difference (based on radii of each constituent element), average atomic volume, and mixing entropy. Chen et al.[347,351] based their descriptors on the fundamental characteristics of the elements such as atomic number, metallic radius, and heat of fusion, as well as thermodynamic and kinetic parameters such a mixing enthalpy, normalized mixing entropy, normalized mismatch entropy, Gibbs free energy of mixing, average atomic volume, and viscosity, according to linear and reciprocal mixing rules. Liu et al.[353] initially selected 23 parameters as candidates for determining GFA, including electronegativity difference, atomic size difference, theoretical density, enthalpy of mixing, mismatch entropy, configurational entropy, bulk modulus, and valence electron concentration, some of which were physical properties and others which were calculated parameters. Xiong et al.[320] used a three-step feature-selection method to screen the normalized feature candidates in their GFA and maximum amorphous diameter dataset. This involved the selection of first-generation features by correlation-based feature selection from among the feature candidates, followed by the selection of second-generation features by comparison of the performance of the variance threshold and the ReliefF algorithm,[354] and finally the determination of

the final feature subset by using wrapper methods (greedy search algorithms). Feng et al.[346] used three types of features or descriptors: 1) statistical information of component properties (i.e., the maximum/minimum/average atomic radius, Pauling electronegativity, elemental bulk modulus, elemental work function, melting point); 2) composition vectors; and 3) parameters derived from empirical criteria such as mixing entropy, mixing enthalpy, atomic size difference, electronegativity difference, and valence electron concentration. Cai et al.[355] used convolutional deep learning algorithms to automatically build a set of descriptors that are relevant to predict a required output.

It is important to mention that when you have too many different features or descriptors, especially compared to the number of training examples (data used to train a deep learning algorithm), it may be desirable to reduce the dimensionality of the features to avoid overfitting, a condition which occurs when a statistical model fits exactly against its training data. When this happens, the algorithm unfortunately cannot perform accurately against unseen data, defeating its purpose. In this case, techniques such as principal component analysis (PCA)[356] can be applied to reduce the dimensionality of the feature vectors, possibly leading to improved model performance.

3.4. Artificial Intelligence Algorithms

The choice of AI algorithm, either a machine learning or a deep learning algorithm,[324,343,357] is a critical step that greatly affects the prediction accuracy, and there is no single algorithm that is appropriate for all tasks. Indeed, selecting an AI algorithm depends on the type of data and the underlying problem to be solved. The algorithm usually has two types of parameters to be configured. First, the parameters for its own configuration specifying structure, architecture, type of learning core function, types of data operations, among others; and second, the parameters (so-called hyperparameters) that can be adjusted during the learning process. The hyperparameters have different ranges and values. Depending on the values of the hyperparameters, the algorithm presents different performance values. Undertaking a performance analysis of the hyperparameters and their relation to the algorithm results is called a grid search. This method performs an exhaustive search for the best combination of hyperparameters for the AI algorithm.[358,359]

AI algorithms follow learned (i.e., preprogrammed) rules to make decisions or generate their own rules through example-based learning, which allows them to establish their own patterns of data representation.[360,361] These patterns allow algorithms to perform well, to some extent, in solving problems of material properties predictions,[362] classifying new sets of materials, or creating new types of amorphous materials.[319] The "learning" stage can be done in supervised, unsupervised, reinforcement, and hybrid formats.

Supervised learning aims to develop a pattern from the training dataset. Once the algorithm is trained, testing can be executed by introducing new data (test data) to perform, for example, a prediction task. For this learning, there is prior knowledge of the desired output y from the input dataset. A function $\hat{f}(\bullet)$ is created that approximates the behavior of a desired function $f(\bullet)$, such that for the desired output $y = f(x)$, an estimated output $\hat{y} = \hat{f}(x)$ is obtained, thus $\hat{y} \cong y$. The desired output belongs to the set of classes of alloys that are defined before learning starts, i.e., $y \in \{1, ..., C\}$, where C equals the total number of existing classes of alloys. Readers can find more details in the work of Muhammad and Yan.[363]

Unsupervised learning aims to develop patterns to create classes from the training dataset. Once the algorithm is trained, an alloy class detection task (or other tasks) can be used for testing. For this learning, there is no prior knowledge of the output. That is, the input alloy data do not have a label or name of its expected alloy class type in the output. In this learning, a function $\hat{f}(\bullet)$ is created that separates the inputs of the dataset x into C distinct classes of alloys, based, for example, on the similarity of the descriptors (i.e., the fundamental characteristics of the elements of the alloy). More detailed information can be found in the work of Chali et al.[364] and Jo et al.[365]

Reinforcement learning aims to develop patterns based on the changes presented in the training dataset during the learning process.[366,367] Once the algorithm has been trained, it can be tested by introducing changes presented in the new data (test data) to work, for example, on a classification task for amorphous and nonamorphous alloys. In reinforcement learning, functions $\hat{f}_k(\bullet)$ are created that approximate the behavior of a desired function $f(\bullet)$, such that for the desired output $y = f(x)$ we obtain a set of estimated outputs $\hat{y}_k = \hat{f}_k(x)$ with $k = \{1, 2, ..., j\}$. From the set of estimated outputs, a selection is made based on the changes presented in the training dataset. For the alloy classes that make up the data, more alloy information is added to these classes that will help in the learning process. This selection of outputs $\{\hat{y}_1, \hat{y}_2, ..., \hat{y}_j\}$ is realized by maximizing a reward function $\hat{g}$ such that $\{\hat{y}_{k_1}, \hat{y}_{k_2}, ..., \hat{y}_{k_j}\} \forall j \in max_i\, \hat{g}$. Then, if the approximation is successful, these selected outputs $\{\hat{y}_{k_1}, \hat{y}_{k_2}, ..., \hat{y}_{k_j}\} \forall j$ will gain confidence through the reward function. In other words, reinforcement learning makes use of data exploration techniques to analyze the changes presented in the dataset during the learning process, and the output is generated according to the maximum possible reward to the selected estimated outputs.

Table 4[319–326,342–347,350–352,357,362,368–378] lists AI efforts in predicting properties, classifying new sets of materials, and creating new types of amorphous alloys. Each of the algorithms described in this table is used with a training set formed by a certain number of features (descriptors of alloy composition), or input parameters, specified by each relevant publication. For training the AI algorithm, the supervised technique is most often used. Most of the studies use cross-validation techniques with tenfold repetition to obtain the artificial intelligence model. Also, most use libraries that already have the AI methods or algorithms implemented in some programming language. The use of these libraries is only required to configure the algorithms. For example, Scikit-learn[379] is a library in Python language for use in machine learning, data mining, and algorithms to process or filter data. Scikit-learn is one of the most used libraries because it has an easy-to-use programming interface and allows different modules to be used in a Python-based project.

To be noted, the training model of most of the AI algorithms uses the k-fold cross-validation technique,[380] which is a resampling process.[381] With this cross-validation technique, an algorithm can be evaluated even with limited data.[348] In this case, a percentage of the training data set (i.e., the validation subset) is

Table 4. Main artificial intelligence algorithms used for amorphous metals. Definitions: C, classification; P, prediction; MG, metallic glass; DT, decision tree; RF, random forest; SVM, support vector machine; LR, logistic regression, KNN, *k*-nearest neighbor; GBDT, gradient boosted decision tree; XGBoost, eXtreme gradient boosting; GFA, glass-forming ability; CV, cross-validation; AM, forming amorphous state; CR, forming crystalline state; VGG, visual geometry group; CNN, convolutional neural network; MRF, materials recovery facility; MLR, multiple linear regression; CBNN, correlation-based neural network; GKRR, Gaussian kernel ridge regression; GB, gradient boosting; PCA, principal component analysis; KNC, *k*-nearest neighbor classifier; DTR, decision tree regressor; RFC, random forest classification; SVC-RBF, radial basis functions; XGBC, gradient boosted decision trees; MLCP, multi-label classification and prediction; FA, firefly algorithm; SVR, support vector regression; RQGPR, ration quadratic kernel-based Gaussian process regression; ExpGPR, exponential kernel Gaussian process regression; CFS, chronic fatigue syndrome; PCC, Pearson correlation coefficient; SBS, sequential backward selection; GP, Gaussian process. ✓: the most frequently used AI algorithms in materials science.

Purpose	Reference	Number of elements in alloy composition	Number of alloys in dataset	Target	Database input parameters	AI algorithms	Training model	Training technique	Library
C and P	[357]	Ternary	5706	MG and non-MG	30	DT, RF✓, SVM, LR, AdaBoost	Grid-search tenfold CV	Supervised	Scikit-learn
P	[324]	Variety	660	D_{max}	T_g, T_x, T_l, D_{max}	KNN, RF, GBDT, XGBoost✓	Grid-search tenfold CV	Supervised	Scikit-learn
P	[347]	Ternary	7200	GFA, T_{rg}	20	RF✓	Tenfold CV	Supervised	Weka
P	[351]	Ternary	7700	GFA, critical casting thickness T_{max}	16	RF✓	CV	Supervised	MATLAB 2020
C and P	[346]	Variety	16 250	AM, CR, GFA, critical cooling rate	–	VGG-like CNN✓	Tenfold CV	Supervised	–
P	[322]	3–9	480	D_{max}: thicknesses between 0.055 and 18 mm	32	MRF, TreeBoost, MLR✓, tree boosting, XGBoost✓ (for nonlinear dependencies)	Tenfold CV	Supervised	Statistical software R
P	[368]	Variety	810	GFA, D_{max}	32	RF regression model	Grid-search, *k*-fold CV	Supervised	Scikit-learn
P	[369]	Variety	667	K criterion, D_{max}	37, 11	Neighborhood components analysis (NCA)	Tenfold CV	Supervised	–
P	[343]	Quaternary	7950	GFA, T_g, D_{max}	–	CBNN	–	Supervised	–
P	[370]	Variety	747	GFA, D_{max}	–	GKRR, RF✓, GB, PCA, PCA-LASSO, PCA-GKRR, $\log_{10}(D_{max})$	Grid-search, fivefold CV inner, fivefold CV outer	Supervised	Scikit-learn
C and P	[342]	Variety	695	GFA	25	KNC, DTR, RFC, SVC-RBF, XGBC, XGBoost✓, MLCP	Tenfold CV	Supervised	Mlstend, Scikit-learn
C and P	[344]	Variety	6732	C: MG and non-MG P: GFA, D_{max}	8	C: FA, RF, SVM, KNN, XGBoost✓ P: FA, fused model approximation (RF, SVM, KNN, XGBoost)	Grid-search, fivefold CV	Supervised	Scikit-learn
P	[371]	5,6,7	7200	P: GFA, critical casting thickness (t_{max})	25	Multilateral-based neural network	–	Supervised	Weka
P	[350]	Ternary	6828	GFA, T_{rg}, elastic modulus k	25	SVR	–	Supervised	–
C and P	[345]	Ternary, 4, 5	5000 MG, 2000 NO-MG + 3000 Virtual NO-MG	P: GFA, lnD C: MG and non-MG	8	C: adaptive boosting (AB)✓, SVM, KNN P: ANN, SVR, RQGPR, ExpGPR, RF✓	Tenfold CV	Supervised	MATLAB R2020
P	[352]	–	442	GFA, D_{max}	4	RF	Tenfold CV	Supervised	Scikit-learn
P	[372]	Variety and Fe-based	667	GFA, D_{max}	10	Linear regression	–	–	–
P	[320]	–	6471, 5934	GFA, D_{max}	20	RF✓, CFS-GFA, PCC, SFS, SBS	100-fold CV	–	Weka
C and P	[321]	Fe-based	252	–	30	C: XGBoost P: XGBoost	Fivefold CV	–	Scikit
P	[326]	Alloy system Ni–Ti–Al	177	GFA	23	RF✓	–	Supervised	Magpie

Table 4. Continued.

Purpose	Reference	Number of elements in alloy composition	Number of alloys in dataset	Target	Database input parameters	AI algorithms	Training model	Training technique	Library
C	[373]	Binary alloy	720 phase region contours and about 7100 text region contours	Classify between phase contours and text contours		GBT, PCA, Pearson correlation coefficient	–	–	–
P	[374]	Variety	219 elastic moduli, 442 D_{max}	Elastic moduli, D_{max}	–	SVR, GP	CV	Supervised	Weka
P	[362]	Al–Co–Cr–Cu–Fe–Ni system	155	Estimate the hardness	–	LRM, PRM, SVR-LK, SVR-PK, SVR-RBFK, RTM, BPNN, knn	CV	–	–
C	[323]	Variety	6315: GFA, 5916: D_{max}, 621: ΔT_x	GFA, D_{max}, ΔT_x, three labels: can form (1) BMG, (2) ribbon, or (3) no glass-forming ability	–	RF✓, REPTrees, and several ensembling techniques	Tenfold CV	Supervised	Weka
–	[319]	Co–V–Zr ternary	6780	GFA metal–metal and metal–metalloid glasses	–	RF	Tenfold CV	–	Weka
–	[375]	Variety	118	Phase selection, Multiprincipal element alloys	5	RNA	Fourfold CV	Supervised	Panda Tensorflow
C	[376]	2	3	Identify the fractal structure at the atomic level, relationship between dynamical properties and T_g	–	Hierarchical cluster analysis, also called segmentation analysis or taxonomy analysis	–	Unsupervised machine learning	Statistic and Machine Toolbox
P and C	[325]	Ternary	25 085 crystalline, 5369 metallic glass	P: bandgap energy, volume, formation energy. P: GFA. C: can and cannot form a metallic glass	145	Decision trees, Rotation forest, RF✓, 10 ML algorithms	Tenfold CV	Supervised	Weka Magpie
–	[377]	Variety	410	GFA, D_{max}	–	Genetic programming	–	–	Fortran 90/95
C	[378]	Variety	594	GFA	11	PCA	–	Supervised	MATLAB R2010a

separated from the training data set to be used in the test and validation of the algorithm, and the remaining percentage data (i.e., the training subset) is used in the training of the algorithm. One of the techniques of cross-validation is called *k*-fold, where the value of *k* indicates the number of separate subsets of data, ensuring that the data in each subset are well distributed and balanced. The value of *k* is generally assigned between 5 and 10. It has been observed that for large values of *k*, the algorithm has smaller biases, but overfitting can occur due to large variance values.[382] The process consists of repeating the training and validation of the algorithm in such a way that each *k*-fold subset of data is used in the training subset. The metric of this technique is the average of the recorded error scores at each repetition. As can be noted in Table 4, the most frequently used AI algorithms in materials science are random forest and eXtreme Gradient Boosting (XGBoost). A discussion of these algorithms and why they are frequently used is presented below.

3.4.1. Random Forest

Random forest is a supervised machine learning algorithm based on a set of independent decision tree algorithms that are trained with random sets of training data and their results combined to obtain the best performance. The algorithm follows what is known as a bagging structure,[383–385] which is organized so that each decision tree is trained with a random subset of data x_i from the training set *X*. Thus, errors between decision trees are compensated to reduce variance. The global result for the solution of the problem, whether it is prediction or classification of materials, is obtained by assembling the results of each of these decision trees, resulting in high performance. Generally, the random forest algorithm models the training set well and can obtain good results for new data by setting an optimal configuration for the algorithm through configuring and establishing the best hyperparameters of the model, including setting the depth of the tree, establishing the minimum number of samples that a final node must have, and establishing the maximum number of final nodes, among others. However, care must be taken with the results in high-dimension trees, as the overall result may be biased. This can come about because the algorithm may not be able to fit the training data properly when the depth level is too low. The algorithm may have a low variance and a low error, but certain patterns may not be characterized because

of the low depth level, which means that a global optimum may not be reached.

This algorithm is used to solve classification and prediction problems. In the case of classification, the results of each of the decision trees are combined using a soft-voting technique. This means that the results with the highest value in each decision tree are given the highest weight. In the case of prediction or regression, the results of each of the decision trees are combined through the mathematical operation of the arithmetic mean. For best performance, some combinations of hyperparameter values can be followed, so-called regularization proposals found in the literature, but it is also possible to create unique hyperparameter regularizations by combining the results and decisions of each set of decision trees. Finally, this algorithm is robust when there are a large number of decision trees because their results are combined to obtain the best performance.[386]

3.4.2. XGBoost

XGBoost is a supervised machine learning algorithm consisting of an optimized gradient boosting decision tree structure.[387] The algorithm uses a training dataset x_i to obtain a target variable y_i as an output using a sequential set of decision trees, with each tree designed to fit the residual of previous trees, allowing reductions in variance and bias. That is, each tree corrects the errors made by the preceding trees and learns from them to output a better result. To minimize errors when adding new trees, the gradient descent algorithm is used. Trees are added until no further improvement can be made and XGBoost processes the data in several blocks in parallel. The algorithm is used in both classification and prediction problems. For a classification problem, a working decision tree assigns more weight to the misclassified samples and less weight to the well classified ones of the previous decision tree. For a prediction problem, a decision tree assigns more weight to the predictions having the largest mean square error of the previous decision tree.[388,389] XGBoost is also being used to predict processing outcomes, thus connecting manufacturing to computational predictions.

3.5. Applications

Some applications using the most widely used AI algorithms (random forest and XGBoost) are described in this section. Chen et al.[347] used the random forest algorithm to improve the GFA through the prediction of the reduced glass transition temperature, T_{rg}, using a group of ternary Mg–Cu–Y alloys. To evaluate glass formation in this group of alloys, they indicated that the T_{rg} prediction value should be greater than 0.4 and obtained an average T_{rg} prediction of 0.635. The authors highlight that through the random forest algorithm they have been able to explore good glass formers without the need to perform numerous trial and error experiments. Similarly, Chen et al.[351] applied the random forest algorithm to obtain the GFA through the prediction of the T_{rg} and the critical casting thickness using a group of ternary Fe–B–Co alloys, as well as the design of new glassy alloys. Zhuang et al.[357] describe five machine learning models to predict the glass formation of metallic glasses using the Scikit-learn library, focusing on optimizing the data description using Pearson's correlation coefficient ($R_{x1,x2}$) and the coefficient of variation (C_v). The study focuses on twelve elemental, thermodynamic, physical, and chemical parameters and shows that the random forest classifier algorithm with tuned hyperparameters presents the best overall performance of 90.02% for classification of metallic and nonmetallic glasses. **Figure 18** details a comparison of predicted glass formation by this random forest optimal model and the measured glass formation reported on the ternary system Cu–Mg–Nd. Ward et al.[323] explored three machine learning methods from the Weka library, including the random forest method, to predict the GFA, D_{max}, and ΔT_x, utilizing a database of 8315 metallic glasses and defining attributes based on statistics of elemental properties of the alloys. **Figure 19**a shows the performance of the random forest classification model for obtaining the GFA with an accuracy of 89% using a receiver operating characteristic curve. Figure 19b,c shows the values of D_{max} and ΔT_x measured experimentally and compared to the values predicted by the random forest method. A correlation coefficient of $R = 0.89$ is indicated for D_{max} and a mean absolute error of 8.8 is indicated for ΔT_x. On the other hand, Mastropietro et al.[322] used the XGBoost algorithm to make a prediction of the maximum critical casting sizes of Fe-based BMGs. The model was characterized by a predicted R^2 of 0.71 and can be used for a priori predictions of critical casting sizes based solely on the atomic composition of the alloy.

While not focusing on metallic glasses, there are other studies that are looking at XGBoost to predict melt pool temperature (see Section 2.2.3), which certainly has applicability in the 3D printing

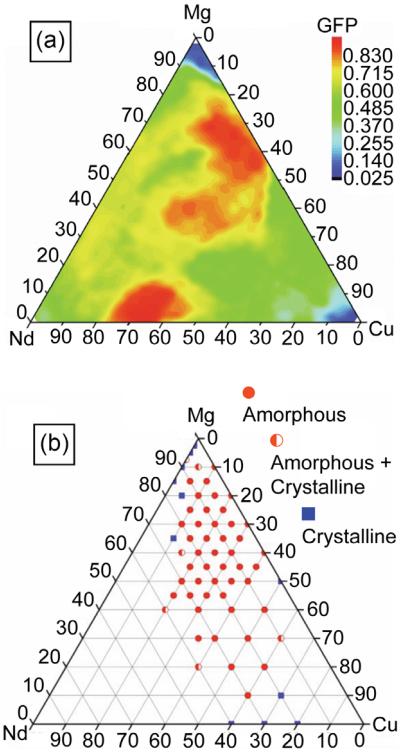

Figure 18. Comparison of a) predicted glass formation and b) measured glass formation for a Cu–Mg–Nd system. Reproduced with permission.[357] Copyright 2021, Elsevier.

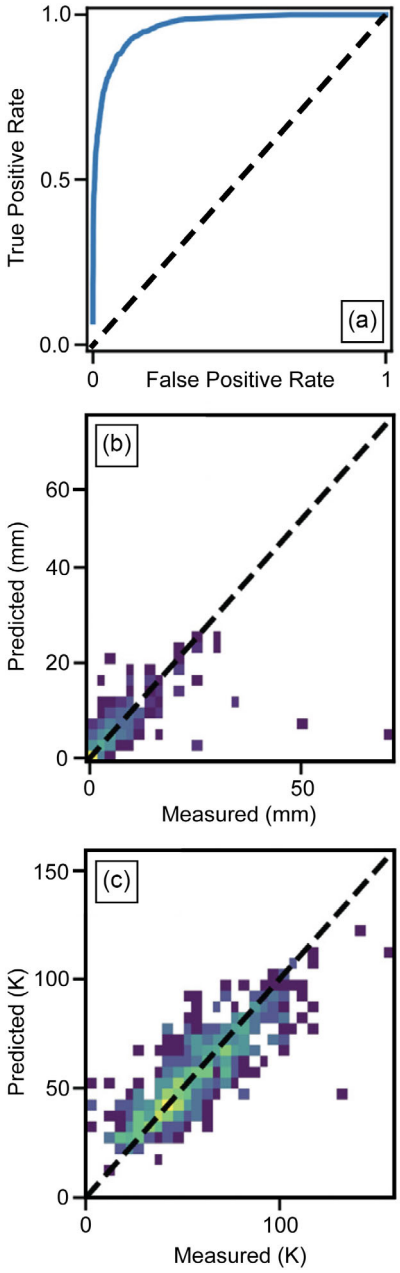

Figure 19. Performance of the Random Forest model for predicting a) the glass forming ability, b) critical casting diameter, and c) supercooled liquid range, using a 10-fold cross-validation test. Reproduced with permission.[323] Copyright 2018, Elsevier.

of metallic glasses. For example, Zhang et al.[390] performed a comparative analysis between experimental measurements of melt pool temperature with respect to those predicted by XGBoost and a long short-term memory (LSTM) algorithm on a nickel-based CarTech 718 superalloy. **Figure 20** illustrates the melt pool temperature with respect to time in a specimen heated using a 350 W laser. It is noted that XGBoost exhibited reasonable predictive capabilities, although the performance of LSTM (not shown) was found to be higher. Nonetheless, the

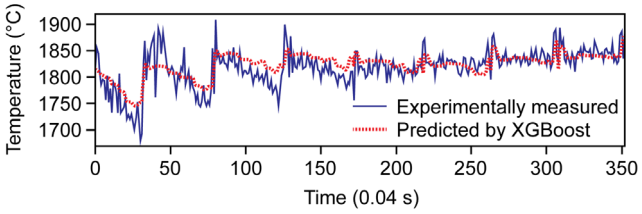

Figure 20. Predicted and observed melt pool temperature in a nickel-based CarTech 718 superalloy during laser engineered net shaping using 350 W laser power and 11 mm s^{-1} scan speed. Reproduced with permission.[390] Copyright 2021, Elsevier.

computational efficiency of XGBoost was approximately 400 times faster compared to LSTM. Thus, performance and efficiency are competing considerations in any AI algorithm. In the work of Xiaowei et al.[324] the XGBoost algorithm presents the highest GFA prediction performance from a database of 660 amorphous alloys, using T_g, T_x, T_ℓ, and D_{max} as attributes. For the three temperatures, the authors specify a high Pearson correlation coefficient (>0.97) between them, whereas they describe a low Pearson correlation coefficient (<0.11) between the temperatures and D_{max}. **Figure 21** illustrates the predicted and measured D_{max}. Here, the closer the points are to the diagonal dashed line, the better the predictions. The XGBoost algorithm has the highest value of the correlation coefficient ($R = 0.755$) and the smallest root mean square error (RMSE = 3.277) for the test set, which means that it has the highest level of accuracy among all the models considered in this work.

Finally, options to merge some machine learning methods have also been proposed, as described by Zhang et al.[344] who evaluate five machine learning methods of the Scikit-learn library. The XGBoost and Fusion methods obtain the highest accuracy values for the prediction of good glass formers and D_{max}, resulting in a coefficient of determination >0.77. The database has 6732 alloys with information on eight physical and chemical attributes. **Figure 22**a presents the experimental results of glass formers in the Al–La–Ni ternary alloy group, and

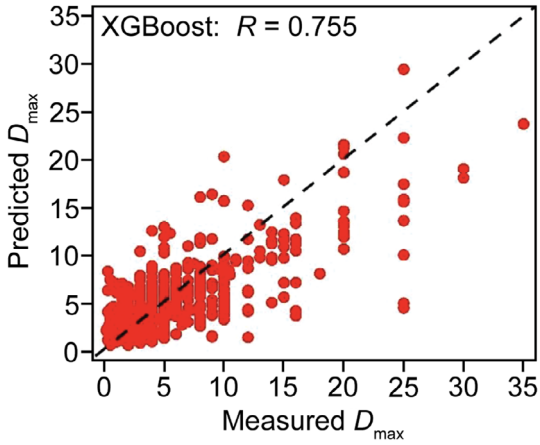

Figure 21. Comparisons of predicted and measured D_{max} obtained using an XGBoost algorithm. Reproduced with permission.[324] Copyright 2021, Elsevier.

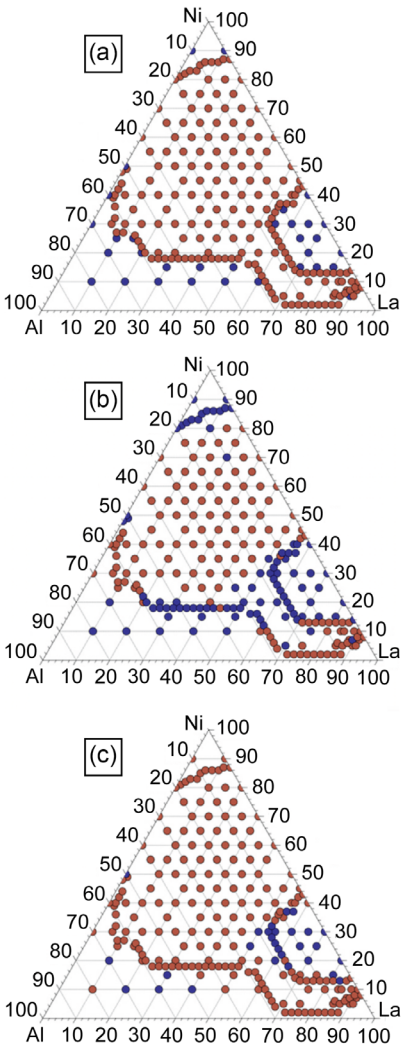

Figure 22. a) Experimental results of good glass formers in the Al–La–Ni system. Predicted results using b) the Random Forest algorithm and c) the XGBoost algorithm. The red dots indicate compositions that result in metallic glasses. The blue dots indicate compositions that do not result in metallic glasses. Reproduced with permission.[344] Copyright 2021, Elsevier.

Figure 22b,c illustrates the predictions from XGBoost and random forest.

3.6. Artificial Intelligence Model Evaluation

The most frequently used metrics for model evaluation are the mean square error and the *R*-squared (coefficient of determination). The mean square error represents the average of the square of the difference between the actual value and the predicted value. This can be interpreted as the fit of the AI algorithm to the data, meaning how close the values given (predicted) by the algorithm are to the actual values. The value of this metric will always be positive, and the value of the perfect error is 0. This metric is a derivable function, which makes it applicable to efficient optimization algorithms.[391–393] The criterion of *R*-squared is often used for descriptive purposes and it shows the variance of the response of the algorithm relative to the input values of the algorithm. A value close to 1 indicates that the AI algorithm is a better fit to the data being represented.[394,395]

4. Final Remarks and Outlook

Amorphous alloys are now becoming commercially relevant,[396] after several decades of basic research, despite their generally higher cost compared to crystalline alloys. As production increases and their use becomes more widespread, one would expect their cost to decrease and new markets to open. As, generally, their hardness is very high compared to the requirements for commercial products, postprocessing (i.e., cutting, drilling, polishing, etc.) is time-intensive and difficult. A goal for some application would then be to reduce hardness in these alloys to improve processability. In this regard, artificial intelligence is having significant impact in the field. Reflecting this trend is the growing number of repositories of amorphous alloys that will allow reproduction of experiments with AI models and the prediction of new compositions. However, there are still current challenges to overcome in the field, such as improving prediction accuracy, reducing dependence on a large amount of data, improving parameter optimization, and finding reliable descriptors that are related closely to the target properties. On the issue of data descriptors, Zhou et al.[345] mention that data descriptor values can also offer important hints about hidden (unknown) structural features of designed alloys, which are also validated by experiments. These findings are important, as they can pave the way toward the computational discovery of chemically complex metallic glasses.

Acknowledgements

O.A.G. acknowledges the National Science Foundation (grant #1911372), and M.S.G.V. and A.A.R.A. acknowledge Instituto Politécnico Nacional (2019-2022 SIP Research Projects) for research support in the preparation of this review. O.A.G. acknowledges the visiting scholar support from Deutscher Akademischer Austauschdienst (DAAD) at Forschungszentrum Jülich during spring 2022, which was partially leveraged in developing the manufacturing sections of this review.

Conflict of Interest

The authors declare no conflict of interest.

Keywords

amorphous metal, artificial intelligence, machine learning, manufacturing, processing

Received: October 16, 2022
Revised: January 10, 2023
Published online:

[1] G. R. Khanolkar, M. B. Rauls, J. P. Kelly, O. A. Graeve, A. M. Hodge, V. Eliasson, *Sci. Rep.* **2016**, *6*, 22568.

[2] K. Hashimoto, *Appl. Surf. Sci.* **2011**, *257*, 8141.
[3] B. Lin, K. Yang, X. Bao, J. Liu, Q. Guo, L. Zhang, Q. Wang, N. Hua, *J. Non-Cryst. Solids* **2022**, *576*, 121231.
[4] S. Schneider, *J. Phys.: Condens. Matter* **2001**, *13*, 7723.
[5] J. F. Löffler, *Intermetallics* **2003**, *11*, 529.
[6] W. H. Wang, C. Dong, C. H. Shek, *Mater. Sci. Eng.: R: Rep.* **2004**, *44*, 45.
[7] A. Inoue, A. Takeuchi, *Acta Mater.* **2011**, *59*, 2243.
[8] D. J. Browne, D. Stratton, M. D. Gilchrist, C. J. Byrne, *Metall. Mater. Trans. A* **2013**, *44*, 2021.
[9] D. C. Hofmann, R. Polit-Casillas, S. N. Roberts, J.-P. Borgonia, R. P. Dillon, E. Hilgemann, J. Kolodziejska, L. Montemayor, J.-O. Suh, A. Hoff, K. Carpenter, A. Parness, W. L. Johnson, A. Kennett, B. Wilcox, *Sci. Rep.* **2016**, *6*, 37773.
[10] M. S. Dambatta, S. Izman, B. Yahaya, J. Y. Lim, D. Kurniawan, *J. Non-Cryst. Solids* **2015**, *426*, 110.
[11] M. Jafary-Zadeh, G. P. Kumar, P. S. Branicio, M. Seifi, J. J. Lewansowski, F. Cui, *J. Funct. Biomater.* **2018**, *9*, 19.
[12] F. Kiani, C. Wen, Y. Li, *Acta Biomater.* **2020**, *103*, 1.
[13] P. Meagher, E. D. O'Cearbhaill, J. H. Byrne, D. J. Browne, *Adv. Mater.* **2016**, *28*, 5755.
[14] J.-Z. Jiang, D. Hofmann, D. J. Jarvis, H.-J. Fecht, *Adv. Eng. Mater.* **2015**, *17*, 761.
[15] J. J. Kruzic, *Adv. Eng. Mater.* **2016**, *18*, 1308.
[16] L. Pei, X. Zhang, Z. Yuan, *J. Renewable Mater.* **2022**, *10*, 969.
[17] S. Xie, P. Huang, J. J. Kruzic, X. Zeng, H. Qian, *Sci. Rep.* **2016**, *6*, 21947.
[18] S.-X. Liang, W. Zhang, W. Wang, G. Jia, W. Yang, L.-C. Zhang, *J. Phys. Chem. Solids* **2019**, *132*, 89.
[19] M. M. Khan, A. Nemati, Z. U. Rahman, U. H. Shah, H. Asgar, W. Haider, *Crit. Rev. Solid State Mater. Sci.* **2018**, *43*, 233.
[20] E. Williams, N. Lavery, *J. Mater. Process. Technol.* **2017**, *247*, 73.
[21] X. Li, *Adv. Eng. Mater.* **2018**, *20*, 1700874.
[22] L. Zhang, H. Huang, *Int. J. Adv. Manuf. Technol.* **2019**, *100*, 637.
[23] Y. Li, Y. Shen, C. Chen, M. C. Leu, H.-L. Tsai, *J. Mater. Process. Technol.* **2017**, *248*, 249.
[24] G. Kumar, A. Desai, J. Schroers, *Adv. Mater.* **2011**, *23*, 461.
[25] D. H. Milanez, L. I. L. Faria, D. R. Leiva, C. S. Kiminami, W. J. Botta, *J. Alloys Compd.* **2017**, *716*, 330.
[26] J. Howard, K. Carlson, D. Chidambaram, *Phys. Rev. Mater.* **2021**, *5*, 040301.
[27] L. Li, J. Li, Y. He, J. Cao, H. Kou, J. Wang, *J. Non-Cryst. Solids* **2020**, *542*, 120105.
[28] F. Spieckermann, D. Şopu, V. Soprunyuk, M. B. Kerber, J. Bednarčík, A. Schökel, A. Rezvan, S. Ketov, B. Sarac, E. Schafler, J. Eckert, *Nat. Commun.* **2022**, *13*, 127.
[29] C. Liao, M. Liu, Q. Zhang, W. Dong, R. Zhao, B. Li, Z. Jiao, J. Song, W. Yao, S. Zhao, H. Bai, W.-H. Wang, *Sci. China Mater.* **2021**, *64*, 979.
[30] X. Liu, X. Mei, J. Qiang, G. E. Remnev, Y. Wang, *Appl. Surf. Sci.* **2014**, *313*, 911.
[31] J. Cao, H. Y. Chen, X. G. Song, J. K. Liu, J. C. Feng, *J. Non-Cryst. Solids* **2013**, *364*, 53.
[32] J. Brechtl, H. Wang, N. A. P. K. Kumar, T. Yang, Y.-R. Lin, H. Bei, J. Neuefeind, W. Dmowski, S. J. Zinkle, *J. Nucl. Mater.* **2019**, *526*, 151771.
[33] F.-Q. Gong, J. Wen, Y.-J. Zhao, J.-B. Qiang, W.-M. Wang, X.-X. Mei, C. Dong, Z.-G. Wang, *J. Nucl. Mater.* **2012**, *429*, 221.
[34] P. Jung, *J. Appl. Phys.* **1999**, *86*, 4876.
[35] Z. Hu, Z. Q. Zhao, Y. D. Wu, T. Lu, J. S. Xing, B. C. Wei, *Vacuum* **2013**, *89*, 142.
[36] H. Kang, X. Ye, J. Wang, S. Pan, L. Wang, *J. Alloys Compd.* **2019**, *780*, 512.
[37] Z. Kovács, E. Schafler, V. Kovács Kis, P. J. Szommer, A. Révész, *J. Non-Cryst. Solids* **2018**, *498*, 25.
[38] O. A. Graeve, R. Kanakala, L. Kaufman, K. Sinha, E. Wang, B. Pearson, G. Rojas-George, J. C. Farmer, *Mater. Lett.* **2008**, *62*, 2988.
[39] A. P. Wang, T. Zhang, J. Q. Wang, *Philos. Mag. Lett.* **2006**, *86*, 5.
[40] J. Schroers, *Adv. Mater.* **2010**, *22*, 1566.
[41] R. Knight, R. W. Smith, D. Apelian, *Int. Mater. Rev.* **1991**, *36*, 221.
[42] E. Soinila, T. Pihlajamäki, S. Bossuyt, H. Hänninen, *Rev. Sci. Instrum.* **2011**, *82*, 073901.
[43] Y. H. Zhao, C. Y. Luo, X. K. Xi, D. Q. Zhao, M. X. Pan, W. H. Wang, *Intermetallics* **2006**, *14*, 1107.
[44] M. Stoica, A. Bàrdos, S. Roth, L. K. Varga, L. Schultz, A. Lovas, J. Eckert, *Adv. Eng. Mater.* **2011**, *13*, 38.
[45] C. Y. Luo, Y. H. Zhao, X. K. Xi, G. Wang, D. Q. Zhao, M. X. Pan, W. H. Wang, S. Z. Kou, *J. Non-Cryst. Solids* **2006**, *352*, 185.
[46] L. M. Andersen, S. Faulhaber, T. Harrington, D. C. Hofmann, H. Cheng, K. S. Vecchio, *J. Non-Cryst. Solids* **2017**, *469*, 70.
[47] O. Biletska, K. J. Laws, M. A. Gibson, M. Ferry, *Metall. Mater. Trans. A* **2014**, *45*, 2352.
[48] T. Nagase, M. Ueda, Y. Umakoshi, *J. Alloys Compd.* **2009**, *485*, 304.
[49] Y. Wang, M. J. Tan, J. Pang, Z. Wang, A. W. E. Jarfors, *Mater. Chem. Phys.* **2012**, *134*, 1079.
[50] Y. Shimpo, S.-I. Yamaura, M. Nishida, H. Kimura, A. Inoue, *J. Membr. Sci.* **2006**, *286*, 170.
[51] G. Zhang, H. Zhang, S. Yue, A. Wang, A. He, R. Cheng, Y. Dong, H. Ni, C.-T. Liu, *J. Non-Cryst. Solids* **2019**, *514*, 108.
[52] V. V. Muhgalin, G. A. Dorofeev, M. A. Eremina, V. I. Lad'yanov, I. V. Sapegina, *Phys. Met. Metall.* **2011**, *112*, 596.
[53] R. Torres, J. A. Verduzco, *Mater. Manuf. Processes* **2003**, *18*, 79.
[54] S. W. Kim, J. Namkung, O. Kwon, *Mater. Sci. Forum* **2012**, *706–709*, 1324.
[55] Y. S. Wang, M. J. Tan, A. W. E. Jarfors, *Mater. Sci. Forum* **2012**, *706–709*, 606.
[56] N. Li, W. Chen, L. Liu, *JOM* **2016**, *68*, 1246.
[57] D. Wang, G. Liao, J. Pan, Z. Tang, P. Peng, L. Liu, T. Shi, *J. Alloys Compd.* **2009**, *484*, 118.
[58] J. A. Bardt, G. R. Bourne, T. L. Schmitz, J. C. Ziegert, W. G. Sawyer, *J. Mater. Res.* **2007**, *22*, 339.
[59] C. T. Pan, T. T. Wu, Y. C. Chang, J. C. Huang, *J. Micromech. Microeng.* **2008**, *18*, 025010.
[60] G. Kumar, H. X. Tang, J. Schroers, *Nature* **2009**, *457*, 868.
[61] M. Ishida, H. Takeda, D. Watanabe, K. Amiya, N. Nishiyama, K. Kita, Y. Saotome, A. Inoue, *Mater. Trans., JIM* **2004**, *45*, 1239.
[62] R. Feltman, Popular Science **2021**, https://www.popsci.com/technology/glass-blowing-process-sustainability/ (accessed: October 2022).
[63] J. Schroers, T. M. Hodges, G. Kumar, H. Raman, A. J. Barnes, Q. Pham, T. A. Waniuk, *Mater. Today* **2011**, *14*, 14.
[64] P. Kollár, J. Bednarčík, S. Roth, H. Grahl, J. Eckert, *J. Magn. Magn. Mater.* **2004**, *278*, 373.
[65] J. Degmova, S. Roth, J. Eckert, H. Grahl, L. Schultz, *Mater. Sci. Eng., A* **2004**, *375–377*, 265.
[66] A. W. Weeber, H. Bakker, *Physica B* **1988**, *153*, 93.
[67] C. C. Koch, *Annu. Rev. Mater. Sci.* **1989**, *19*, 121.
[68] M. A. Taha, R. A. Youness, M. F. Zawrah, *Int. J. Miner. Metall. Mater.* **2019**, *26*, 1047.
[69] P. S. Gilman, J. S. Benjamin, *Annu. Rev. Mater. Sci.* **1983**, *13*, 279.
[70] G. Mucsi, *Chem. Eng. Res. Des.* **2019**, *148*, 460.
[71] B. S. Murty, S. Ranganathan, *Int. Mater. Rev.* **1998**, *43*, 101.
[72] R. Sundaresan, F. H. Froes, *JOM* **1987**, *39*, 22.
[73] C. Suryanarayana, *Prog. Mater. Sci.* **2001**, *46*, 1.
[74] M. H. Enayati, F. A. Mohamed, *Int. Mater. Rev.* **2014**, *59*, 394.
[75] S. Seshan, J. Kaneko, *Adv. Compos. Mater.* **2012**, *2*, 153.
[76] H. V. Atkinson, S. Davies, *Metall. Mater. Trans. A* **2000**, *31*, 2981.
[77] A. Inoue, L. Arnberg, M. Oguchi, U. Backmark, N. Bäckström, T. Masumoto, *Mater. Sci. Eng.* **1987**, *95*, 101.

[78] K. Matsuki, A. Inoue, H. M. Kimura, T. Masumoto, *Mater. Sci. Eng.* **1988**, *97*, 47.
[79] Z. Wang, K. G. Prashanth, K. B. Surreddi, C. Suryanarayana, J. Eckert, S. Scudino, *Materialia* **2018**, *2*, 157.
[80] I. Börner, J. Eckert, *Scr. Mater.* **2001**, *45*, 237.
[81] M. Calin, H. Grahl, M. Adam, J. Eckert, L. Schultz, *J. Mater. Sci.* **2004**, *39*, 5295.
[82] M. Sherif El-Eskandarany, S. Ishihara, W. Zhang, A. Inoue, *Metall. Mater. Trans. A* **2005**, *36*, 141.
[83] M. Sherif El-Eskandarany, A. Inoue, *Metall. Mater. Trans. A* **2006**, *37*, 2231.
[84] M. Sherif El-Eskandarany, A. Inoue, *J. Mater. Res.* **2006**, *21*, 976.
[85] D. V. Louzguine, Y. Kawamure, A. Inoue, *Mater. Sci. Technol* **1999**, *15*, 583.
[86] E. Y. Kang, Y. B. Kim, K. Y. Kim, Y. H. Chung, *J. Appl. Phys.* **2006**, *99*, 08F111.
[87] P.-Y. Lee, S.-S. Hung, J.-T. Hsieh, Y.-L. Lin, C.-K. Lin, *Intermetallics* **2002**, *10*, 1277.
[88] P. Y. Lee, M. C. Kao, C. K. Lin, J. C. Huang, *Intermetallics* **2006**, *14*, 994.
[89] P. Y. Lee, W. C. Liu, C. K. Lin, J. C. Huang, *Mater. Sci. Eng., A* **2007**, *449–451*, 1095.
[90] P. Y. Lee, C. Lo, J. S. C. Jang, *J. Alloys Compd.* **2007**, *434–435*, 354.
[91] H.-M. Lin, C.-Y. Chen, C.-Y. Tsay, C.-F. Hsu, P.-Y. Lee, *J. Alloys Compd.* **2010**, *504*, S110.
[92] X. Wei, F. Han, X. Wang, X. Wang, C. Wen, *J. Alloys Compd.* **2010**, *501*, 164.
[93] T. He, V. Ciftci, V. Uhlenwinkel, S. Scudino, *J. Manuf. Mater. Process.* **2021**, *5*, 23.
[94] O. A. Graeve, M. S. Saterlie, R. Kanakala, S. Diaz de la Torre, J. C. Farmer, *Scr. Mater.* **2013**, *69*, 143.
[95] A. Yazdani, G. W. H. Höhne, S. T. Misture, O. A. Graeve, *PLoS One* **2020**, *15*, 0234774.
[96] I. Gallino, M. B. Shah, R. Busch, *Acta Mater.* **2007**, *55*, 1367.
[97] B. A. Legg, J. Schroers, R. Busch, *Acta Mater.* **2007**, *55*, 1109.
[98] B. Bochtler, O. Gross, I. Gallino, R. Busch, *Acta Mater.* **2016**, *118*, 129.
[99] J. Q. Wang, Y. Shen, J. H. Perepezko, M. D. Ediger, *Acta Mater.* **2016**, *104*, 25.
[100] Y. J. Kim, R. Busch, W. L. Johnson, A. J. Rulison, W. K. Rhim, *Appl. Phys. Lett.* **1996**, *68*, 1057.
[101] J. F. Löffler, J. Schroers, W. L. Johnson, *Appl. Phys. Lett.* **2000**, *77*, 681.
[102] R. Busch, A. Masuhr, W. L. Johnson, *Mater. Sci. Eng., A* **2001**, *304–306*, 97.
[103] C. C. Hays, J. Schroers, W. L. Johnson, T. J. Rathz, R. W. Hyers, J. R. Rogers, M. B. Robinson, *Appl. Phys. Lett.* **2001**, *79*, 1605.
[104] S. Mukherjee, Z. Zhou, J. Schroers, W. L. Johnson, W. K. Rhim, *Appl. Phys. Lett.* **2004**, *84*, 5010.
[105] J. P. Kelly, O. A. Graeve, *JOM* **2015**, *67*, 29.
[106] O. Guillon, J. Gonzalez-Julian, B. Dargatz, T. Kessel, G. Schierning, J. Räthel, M. Hermann, *Adv. Eng. Mater.* **2014**, *16*, 830.
[107] E. Novitskaya, K. Karandikar, K. Cummings, M. Mecartney, O. A. Graeve, *J. Mater. Res. Tech.* **2021**, *11*, 823.
[108] U. Santoro, E. Novitskaya, K. Karandikar, H. E. Khalifa, O. A. Graeve, *Mater. Lett.* **2019**, *241*, 123.
[109] J. T. Cahill, V. R. Vasquez, S. T. Misture, D. Edwards, O. A. Graeve, *ACS Appl. Mater. Interfaces* **2017**, *9*, 37357.
[110] J. T. Cahill, M. Alberga, J. Bahena, C. Pisano, R. Borja-Urby, V. R. Vasquez, D. Edwards, S. T. Misture, O. A. Graeve, *Cryst. Growth Des.* **2017**, *17*, 3450.
[111] J. P. Kelly, O. A. Graeve, *Acta Mater.* **2015**, *84*, 472.
[112] K. Sinha, B. Pearson, S. R. Casolco, J. E. Garay, O. A. Graeve, *J. Am. Ceram. Soc.* **2009**, *92*, 2504.
[113] J. T. Cahill, J. P. Kelly, E. Novitskaya, M. McKee, J. A. Bahena, O. A. Graeve, *J. Am. Ceram. Soc.* **2019**, *102*, 595.
[114] J. P. Kelly, S. M. Fuller, K. Seo, E. Novitskaya, V. Eliasson, A. M. Hodge, O. A. Graeve, *Mater. Des.* **2016**, *93*, 26.
[115] Z.-H. Zhang, Z.-F. Liu, J.-F. Lu, X.-B. Shen, F.-C. Wang, Y.-D. Wang, *Scr. Mater.* **2014**, *81*, 56.
[116] B. Shen, A. Inoue, *J. Mater. Res.* **2003**, *18*, 2115.
[117] C. K. Kim, H. S. Lee, S. Y. Shin, J. C. Lee, D. H. Kim, S. Lee, *Mater. Sci. Eng., A* **2005**, *406*, 293.
[118] G. Xie, D. V. Louzguine-Luzgin, H. Kimura, A. Inoue, *Appl. Phys. Lett.* **2007**, *90*, 241902.
[119] H. Ding, Z. Zhao, J. Jin, L. Deng, P. Gong, X. Wang, *J. Alloys Compd.* **2021**, *850*, 156724.
[120] T.-S. Kim, J.-K. Lee, H.-J. Kim, J.-C. Bae, *Mater. Sci. Eng., A* **2005**, *402*, 228.
[121] J. K. Lee, H. J. Kim, T. S. Kim, S. Y. Shin, Y. C. Kim, J. C. Bae, *J. Mater. Process. Technol.* **2007**, *187–188*, 801.
[122] Y. T. Feng, X. H. Wang, G. Wang, Q. Li, *Ferroelectrics* **2016**, *505*, 190.
[123] Z. H. Chu, H. Kato, G. Q. Xie, G. Y. Yuan, W. J. Ding, A. Inoue, *J. Non-Cryst. Solids* **2012**, *358*, 1263.
[124] Z. Chang, W. Wang, Y. Ge, J. Zhou, P. Dong, Z. Cui, *J. Alloys Compd.* **2019**, *780*, 220.
[125] P. Drescher, K. Witte, B. Yang, R. Steuer, O. Kessler, E. Burkel, C. Schick, H. Seitz, *J. Alloys Compd.* **2016**, *667*, 109.
[126] G. Xie, F. Qin, S. Zhu, A. Inoue, *Intermetallics* **2012**, *29*, 99.
[127] B. Zheng, D. Ashford, Y. Zhou, S. N. Mathaudhu, J.-P. Delplanque, E. J. Lavernia, *Acta Mater.* **2013**, *61*, 4414.
[128] S. Nagireddi, D. Arvindha Babu, B. Srinivasarao, B. Majumdar, *J. Alloys Compd.* **2021**, *876*, 160057.
[129] M. Suárez, D. Fernández-González, L. A. Díaz, F. Diologent, L. F. Verdeja, A. Fernández, *Intermetallics* **2021**, *139*, 107366.
[130] T. Paul, S. P. Harimkar, *J. Appl. Phys.* **2016**, *120*, 134901.
[131] G. He, Q. Chen, *J. Alloys Compd.* **2019**, *797*, 213.
[132] S. P. Harimkar, S. R. Paital, A. Singh, R. Aalund, N. B. Dahotre, *J. Non-Cryst. Solids* **2009**, *355*, 2179.
[133] X. P. Li, M. Yan, G. B. Schaffer, M. Qian, *Intermetallics* **2013**, *39*, 69.
[134] L. Zarazúa-Villalobos, N. Mary, J. Soo-Hyun, K. Ogawa, H. Kato, Y. Ichikawa, *J. Alloys Compd.* **2021**, *880*, 160399.
[135] S. Nowak, L. Perrière, L. Dembinski, S. Tusseau-Nenez, Y. Champion, *J. Alloys Compd.* **2011**, *509*, 1011.
[136] L. H. Liu, C. Yang, Y. G. Yao, F. Wang, W. W. Zhang, Y. Long, Y. Y. Li, *Intermetallics* **2015**, *66*, 1.
[137] S. Cardinal, J. M. Pelletier, J. C. Qiao, G. Bonnefont, G. Xie, *Mater. Sci. Eng., A* **2016**, *677*, 116.
[138] I.-C. Cheng, J. P. Kelly, E. Novitskaya, V. Eliasson, A. M. Hodge, O. A. Graeve, *Adv. Eng. Mater.* **2018**, *20*, 1800023.
[139] T. Q. Phan, J. P. Kelly, M. E. Kassner, V. Eliasson, O. A. Graeve, A. M. Hodge, *J. Metall.* **2016**, *2016*, 6508597.
[140] C. Manière, E. Nigito, L. Durand, A. Weibel, Y. Beynet, C. Estournès, *Powder Technol.* **2017**, *320*, 340.
[141] T. Voisin, L. Durand, N. Karnatak, S. Le Gallet, M. Thomas, Y. Le Berre, J.-F. Castagné, A. Couret, *J. Mater. Process. Technol.* **2013**, *213*, 269.
[142] C. Manière, E. Torresani, E. A. Olevsky, *Materials* **2019**, *12*, 557.
[143] H. Liu, Q. Jiang, J. Huo, Y. Zhang, W. Yang, X. Li, *Addit. Manuf.* **2020**, *36*, 101568.
[144] H. R. Lashgari, M. Ferry, S. Li, *J. Mater. Sci. Technol.* **2022**, *119*, 131.
[145] M. Vaezi, H. Seitz, S. Yang, *Int. J. Adv. Manuf. Tech.* **2013**, *67*, 1721.
[146] W. E. King, A. T. Anderson, R. M. Ferencz, N. E. Hodge, C. Kamath, S. A. Khairallah, A. M. Rubenchik, *Appl. Phys. Lett.* **2015**, *2*, 041304.
[147] R. J. Hebert, *J. Mater. Sci.* **2016**, *51*, 1165.
[148] A. Lores, N. Azurmendi, I. Agote, E. Zuza, *Powder Metall.* **2019**, *62*, 267.

[149] C. Y. Yap, C. K. Chua, Z. L. Dong, Z. H. Liu, D. Q. Zhang, L. E. Loh, S. L. Sing, *Appl. Phys. Rev.* **2015**, *2*, 041101.
[150] S. F. S. Shirazi, S. Gharehkhani, M. Mehrali, H. Yarmand, H. S. C. Metselaar, N. A. Kadri, N. A. A. Osman, *Sci. Technol. Adv. Mater.* **2015**, *16*, 033502.
[151] W. Gao, Y. Zhang, D. Ramanujan, K. Ramani, Y. Chen, C. B. Williams, C. C. L. Wang, Y. C. Shin, S. Zhang, P. D. Zavatttieri, *Comput. Aided Des.* **2015**, *69*, 65.
[152] W. J. Sames, F. A. List, S. Pannala, R. R. Dehoff, S. S. Babu, *Int. Mater. Rev.* **2016**, *61*, 315.
[153] L. Hirt, A. Reiser, R. Spolenak, T. Zambelli, *Adv. Mater.* **2017**, *29*, 201604211.
[154] P. K. Gokuldoss, S. Kolla, J. Eckert, *Materials* **2017**, *10*, 672.
[155] A. Bandyopadhyay, K. D. Traxel, *Addit. Manuf.* **2018**, *22*, 758.
[156] A. Mitchell, U. Lafont, M. Hołyńska, C. Semprimoschnig, *Addit. Manuf.* **2018**, *24*, 606.
[157] L. E. Murr, *Metall. Microstruct. Anal.* **2018**, *7*, 103.
[158] S. Cooke, K. Ahmadi, S. Willerth, R. Herring, *J. Manuf. Processes* **2020**, *57*, 978.
[159] J. J. Beaman, D. L. Bourell, C. C. Seepersad, D. Kovar, *J. Manuf. Sci. Eng.* **2020**, *142*, 110812.
[160] W. Mycroft, M. Katzman, S. Tammas-Williams, E. Hernandez-Nava, G. Panoutsos, I. Todd, V. Kadirkamanathan, *J. Intell. Manuf.* **2020**, *31*, 1769.
[161] D. Gu, X. Shi, R. Poprawe, D. L. Bourell, R. Setchi, J. Zhu, *Science* **2021**, *372*, eabg1487.
[162] M. Bhuvanesh Kumar, P. Sathiya, *Thin Walled Struct.* **2021**, *159*, 107228.
[163] G. Liu, X. Zhang, X. Chen, Y. He, L. Cheng, M. Huo, J. Yin, F. Hao, S. Chen, P. Wang, S. Yi, L. Wan, Z. Mao, Z. Chen, X. Wang, Z. Cao, J. Lu, *Mater. Sci. Eng.: R: Rep.* **2021**, *145*, 100596.
[164] A. Vafadar, F. Guzzomi, A. Rassau, K. Hayward, *Appl. Sci.* **2021**, *11*, 1213.
[165] S. M. Hashemi, S. Parvizi, H. Baghbanijavid, A. T. L. Tan, M. Nematollahi, A. Ramazani, N. X. Fang, M. Elahinia, *Int. Mater. Rev.* **2022**, *67*, 1.
[166] S. A. M. Tofail, E. P. Koumoulos, A. Bandyopadhyay, S. Bose, L. O'Donoghue, C. Charitidis, *Mater. Today* **2018**, *21*, 22.
[167] J. P. Best, J. Ast, B. Li, M. Stolpe, R. Busch, F. Yang, X. Li, J. Michler, J. J. Kruzic, *Mater. Sci. Eng., A* **2020**, *770*, 138535.
[168] V. Pacheco, D. Karlsson, J. J. Marattukalam, M. Stolpe, B. Hjörvarsson, U. Jansoon, M. Sahlberg, *J. Alloys Compd.* **2020**, *825*, 153995.
[169] B. Zheng, Y. Zhou, J. E. Smugeresky, E. J. Lavernia, *Metall. Mater. Trans. A* **2009**, *40*, 1235.
[170] E. Williams, E. B. Brousseau, *J. Mater. Process. Technol.* **2016**, *232*, 34.
[171] Y. Zhang, X. Lin, L. Wei, F. Liu, W. Huang, *Intermetallics* **2016**, *76*, 1.
[172] Y. Lu, H. Zhang, H. Li, H. Xu, G. Huang, Z. Qin, X. Lu, *J. Non-Cryst. Solids* **2017**, *461*, 12.
[173] D. Ouyang, N. Li, W. Xing, J. Zhang, L. Liu, *Intermetallics* **2017**, *90*, 128.
[174] Y. Lu, Y. Huang, J. Wu, X. Lu, Z. Qin, D. Daisenberger, Y.-L. Chiu, *Intermetallics* **2018**, *103*, 67.
[175] J. Lindwall, A. Malmelöv, A. Lundbäck, L.-E. Lindgren, *JOM* **2018**, *70*, 1598.
[176] D. Ouyang, W. Xing, N. Li, Y. Li, L. Liu, *Addit. Manuf.* **2018**, *23*, 246.
[177] W. Xing, D. Ouyang, N. Li, L. Liu, *Intermetallics* **2018**, *103*, 101.
[178] Y. Zhang, H. Liu, J. Mo, M. Wang, Z. Chen, Y. He, W. Yang, C. Tang, *Comp. Mater. Sci.* **2018**, *150*, 62.
[179] J. Lindwall, V. Pacheco, M. Sahlberg, A. Lundbäck, L.-E. Lindgren, *Addit. Manuf.* **2019**, *27*, 345.
[180] Y. Zhang, H. Liu, J. Mo, M. Wang, Z. Chen, Y. He, W. Yang, C. Tang, *Phys. Chem. Chem. Phys.* **2019**, *21*, 12406.
[181] Q. Jiang, H. Liu, J. Li, D. Yang, Y. Zhang, W. Yang, *Addit. Manuf.* **2020**, *34*, 101369.
[182] H. Y. Jung, S. J. Choi, K. G. Prashanth, M. Stoica, S. Scudino, S. Yi, U. Kühn, D. H. Kim, K. B. Kim, J. Eckert, *Mater. Des.* **2015**, *86*, 703.
[183] S. Pauly, C. Schricker, S. Scudino, L. Deng, U. Kühn, *Mater. Des.* **2017**, *135*, 133.
[184] J. P. Best, H. E. Ostergaard, B. Li, M. Stolpe, F. Yang, K. Nomoto, M. T. Hasib, O. Muránsky, R. Busch, X. Li, J. J. Kruzic, *Addit. Manuf.* **2020**, *36*, 101416.
[185] J. Shi, S. Ma, S. Wei, J. P. Best, M. Stolpe, A. Beckmann, S. Mostafavi, S. Korte-Kerzel, B. Markert, *Mater. Charact.* **2020**, *162*, 110178.
[186] D. C. Hofmann, P. Bordeenithikasem, A. Pate, S. N. Roberts, E. Vogli, *Adv. Eng. Mater.* **2018**, *20*, 1800433.
[187] H. Sun, K. M. Flores, *Metall. Mater. Trans. A* **2010**, *41*, 1752.
[188] H. Sun, K. M. Flores, *Intermetallics* **2011**, *19*, 1538.
[189] V. K. Balla, A. Bandyopadhyay, *Surf. Coat. Technol.* **2010**, *205*, 2661.
[190] X. P. Li, C. W. Kang, H. Huang, T. B. Sercombre, *Mater. Des.* **2014**, *63*, 407.
[191] X. P. Li, M. P. Roberts, S. O'Keeffe, T. B. Sercombe, *Mater. Des.* **2016**, *112*, 217.
[192] Ł. Żrodowski, B. Wysocki, R. Wróblewski, A. Krawczyńska, B. Adamczyk-Cieślak, J. Zdunek, P. Błyskun, J. Ferenc, M. Leonowicz, W. Święszkowski, *J. Alloys Compd.* **2019**, *771*, 769.
[193] N. T. Aboulkhair, N. M. Everitt, I. Ashcroft, C. Tuck, *Addit. Manuf.* **2014**, *1–4*, 77.
[194] K. G. Prashanth, S. Scudino, T. Maity, J. Das, J. Eckert, *Mater. Res. Lett.* **2017**, *5*, 386.
[195] B. Utela, D. Storti, R. Anderson, M. Ganter, *J. Manuf. Processes* **2008**, *10*, 96.
[196] M. G. Ozden, N. A. Morley, *Magnetochemistry* **2021**, *7*, 20.
[197] Q. J. Chen, S. B. Guo, X. J. Yang, X. L. Zhou, X. Z. Hua, X. H. Zhu, Z. Duan, *Phys. Procedia* **2013**, *50*, 297.
[198] J. B. Cheng, Z. H. Wang, B. S. Xu, *J. Therm. Spray Technol.* **2012**, *21*, 1025.
[199] J. Cheng, D. Liu, X. Liang, Y. Chen, *Tribol. Lett.* **2015**, *60*, 22.
[200] S. Katakam, V. Kumar, S. Santhanakrishnan, R. Rajamure, P. Samimi, N. B. Dahotre, *J. Alloys Compd.* **2014**, *604*, 266.
[201] S. S. Raiman, R. T. Mayes, J. M. Kurley, R. Parrish, E. Vogli, *Sol. Energy Mater. Sol. Cells* **2019**, *201*, 110028.
[202] H. Sahasrabudhe, A. Bandyopadhyay, *Surf. Coat. Technol.* **2014**, *240*, 286.
[203] M. Tavoosi, A. Barahimi, *Surf. Interfaces* **2017**, *8*, 103.
[204] N. Sohrabi, R. Santhanu Panikar, J. Jhabvala, A. Roda Buch, S. Mischler, R. E. Logé, *Surf. Coat. Technol.* **2020**, *400*, 126223.
[205] S. S. Joshi, S. Katakam, H. Singh Arora, S. Mukherjee, N. B. Dahotre, *Crit. Rev. Solid State Mater. Sci.* **2016**, *41*, 1.
[206] C. U. Hardwicke, Y.-C. Lau, *J. Therm. Spray Technol.* **2013**, *22*, 564.
[207] L. Pawlowski, *Surf. Coat. Technol.* **2009**, *203*, 2807.
[208] L.-M. Berger, *Int. J. Refract. Met. Hard Mater.* **2015**, *49*, 350.
[209] R. S. Lima, B. R. Marple, *J. Therm. Spray Technol.* **2007**, *16*, 40.
[210] A. Killinger, R. Gadow, G. Mauer, A. Guignard, R. Vaßen, D. Stöver, *J. Therm. Spray Technol.* **2011**, *20*, 677.
[211] S. Chandra, P. Fauchais, *J. Therm. Spray Technol.* **2009**, *18*, 148.
[212] A. Meghwal, A. Anupam, B. S. Murty, C. C. Berndt, R. Sankar Kottada, A. Siao Ming Ang, *J. Therm. Spray Technol.* **2020**, *29*, 857.
[213] C.-J. Li, G.-J. Yang, C.-X. Li, *J. Therm. Spray Technol.* **2013**, *22*, 192.
[214] J. Matějíček, P. Chráska, J. Linke, *J. Therm. Spray Technol.* **2007**, *16*, 64.
[215] N. Cinca, C. R. Camello Lima, J. M. Guilemany, *J. Mater. Res. Technol.* **2013**, *2*, 75.
[216] P. Fauchais, G. Montavon, R. S. Lima, B. R. Marple, *J. Phys. D: Appl. Phys.* **2011**, *44*, 093001.

[217] J. A. Gan, C. C. Berndt, *Int. Mater. Rev.* **2015**, *60*, 195.
[218] J. Henao, C. Poblano-Salas, M. Monsalve, J. Corona-Castuera, O. Barceinas-Sanchez, J. Mater, *Res. Technol.* **2019**, *8*, 4965.
[219] W. Guo, Y. Wu, J. Zhang, S. Hong, G. Li, G. Ying, J. Guo, Y. Qin, *J. Therm. Spray Technol.* **2014**, *23*, 1157.
[220] B. Huang, C. Zhang, G. Zhang, H. Liao, *Surf. Coat. Technol.* **2019**, *377*, 124896.
[221] J. W. Luster, G. R. Heath, P. A. Kammer, *Mater. Manuf. Processes* **1996**, *11*, 855.
[222] J. C. Farmer, J. J. Haslam, S. D. Day, T. Lian, C. K. Saw, P. D. Hailey, J.-S. Choi, R. B. Regak, N. Yang, J. H. Payer, J. H. Perepezko, K. Hildal, E. J. Lavernia, L. Ajdelsztajn, D. J. Branagan, E. J. Buffa, L. F. Aprigliano, *J. Mater. Res.* **2007**, *22*, 2297.
[223] X. Q. Liu, Y. G. Zheng, X. C. Chang, W. L. Hou, J. Q. Wang, Z. Tang, A. Burgess, *J. Alloys Compd.* **2009**, *484*, 300.
[224] Y. H. Yoo, S. H. Lee, J. G. Kim, J. S. Kim, C. Lee, *J. Alloys Compd.* **2008**, *461*, 304.
[225] N. C. Wu, K. Chen, W. H. Sun, J. Q. Wang, *Surf. Eng.* **2019**, *35*, 37.
[226] H. Zhang, Y. Hu, G. Hou, Y. An, G. Liu, *J. Non-Cryst. Solids* **2014**, *406*, 37.
[227] M. Sadeghilaridjani, Y. C. Yang, V. Hasannaeimi, C. Mahajan, S. Jha, M. Pole, Z. Xia, S. Mukherjee, *ACS Appl. Mater. Interfaces* **2021**, *13*, 9260.
[228] J. Du, B. Tian, L. Duan, W. Ming, K. Liu, W. He, *Int. J. Adv. Manuf. Technl.* **2022**, *120*, 2879.
[229] M. Bakkal, A. J. Shih, R. O. Scattergood, *Int. J. Mach. Tools Manuf.* **2004**, *44*, 915.
[230] M. Bakkal, A. J. Shih, S. B. McSpadden, C. T. Liu, R. O. Scattergood, *Int. J. Mach. Tools Manuf.* **2005**, *45*, 741.
[231] K. Fujita, Y. Moroshita, N. Nishiyama, H. Kimura, A. Inoue, *Mater. Trans.* **2005**, *46*, 2856.
[232] M. Bakkal, A. J. Shih, S. B. McSpadden, R. O. Scattergood, *Int. J. Mach. Tools Manuf.* **2005**, *45*, 863.
[233] M. Bakkal, A. J. Shih, R. O. Scattergood, C. T. Liu, *Scr. Mater.* **2004**, *50*, 583.
[234] M. Bakkal, C. T. Liu, T. R. Watkins, R. O. Scattergood, A. J. Shih, *Intermetallics* **2004**, *12*, 195.
[235] M. Bakkal, *J. Non-Cryst. Solids* **2009**, *355*, 2220.
[236] M. Bakkal, E. Serbest, I. Karipçin, A. T. Kuzu, U. Karagüzel, B. Derin, *Adv. Manuf.* **2015**, *3*, 282.
[237] M. Q. Jiang, L. H. Dai, *Acta Mater.* **2009**, *57*, 2730.
[238] X. Chen, J. Xiao, Y. Zhu, R. Tian, X. Shu, J. Xu, *Mater. Des.* **2017**, *136*, 1.
[239] W. D. Liu, L. M. Ye, K. X. Liu, *J. Appl. Phys.* **2011**, *109*, 043109.
[240] I. Quintana, T. Dobrev, A. Aranzabe, G. Lalev, S. Dimov, *Appl. Surf. Sci.* **2009**, *255*, 6641.
[241] H.-K. Lin, C.-J. Lee, T.-T. Hu, C.-H. Li, J. C. Huang, *Opt. Lasers Eng.* **2012**, *50*, 883.
[242] H. Huang, J. Yan, *J. Micromech. Microeng.* **2017**, *27*, 075007.
[243] Y. Qian, H. Huang, M. Jiang, J. Yan, *Appl. Surf. Sci.* **2022**, *577*, 151976.
[244] N. M. Abbas, D. G. Solomon, M. F. Bahari, *Int. J. Mach. Tools Manuf.* **2007**, *47*, 1214.
[245] A. Banu, M. Y. Ali, *Int. J. Eng. Mater. Manuf.* **2016**, *1*, 3.
[246] S. Kumar, R. Singh, T. P. Singh, B. L. Sethi, *J. Mater. Process. Technol.* **2009**, *209*, 3675.
[247] F. N. Leão, I. R. Pashby, *J. Mater. Process. Technol* **2004**, *149*, 341.
[248] K. H. Ho, S. T. Newman, *Int. J. Mach. Tools Manuf.* **2003**, *43*, 1287.
[249] A. Kumar, S. Maheshwari, C. Sharma, N. Beri, *Mater. Manuf. Processes* **2010**, *25*, 1166.
[250] S. Chakraborty, V. Dey, S. K. Ghosh, *Precis. Eng.* **2015**, *40*, 1.
[251] W. Ming, Z. Xie, J. Ma, J. Du, G. Zhang, C. Cao, Y. Zhang, *J. Manuf. Processes* **2021**, *72*, 375.
[252] K. H. Ho, S. T. Newman, S. Rahimifard, R. D. Allen, *Int. J. Mach. Tools Manuf.* **2004**, *44*, 1247.
[253] A. Y. Joshi, A. Y. Joshi, *Heliyon* **2019**, *5*, e02963.
[254] S. H. Yeo, P. C. Tan, E. Aligiri, S. B. Tor, N. H. Loh, *Mater. Manuf. Processes* **2009**, *24*, 1242.
[255] S.-F. Hsieh, S.-L. Chen, M.-H. Lin, S.-F. Ou, W.-T. Lin, M.-S. Huang, *J. Mater. Res.* **2013**, *28*, 3177.
[256] R. Sueptitz, K. Tschulik, C. Becker, M. Stoica, M. Uhlemann, J. Eckert, A. Gebert, *J. Mater. Res.* **2012**, *27*, 3033.
[257] K. M. Cole, D. W. Kirk, C. V. Singh, S. J. Thorpe, *J. Manuf. Processes* **2017**, *25*, 227.
[258] S. Horn, S. Oswald, M. Stoica, M. Uhlemann, A. Gebert, *J. Mater. Res.* **2015**, *30*, 3493.
[259] J. A. Koza, R. Sueptitz, M. Uhlemann, L. Schultz, A. Gebert, *Intermetallics* **2011**, *19*, 437.
[260] H. Huang, J. Yan, *Appl. Surf. Sci.* **2015**, *355*, 1306.
[261] P. S. Ng, S. A. Kong, S. H. Yeo, *Int. J. Adv. Manuf. Technol.* **2017**, *90*, 2549.
[262] L. Meng, W. Zeng, D. Zhu, *Electrochim. Acta* **2017**, *233*, 274.
[263] L. Meng, Y. Zeng, X. Fang, D. Zhu, *Intermetallics* **2017**, *81*, 16.
[264] Y. Zeng, L. Meng, X. Fang, *J. Electrochem. Soc.* **2017**, *164*, E408.
[265] S. Reyntjens, R. Puers, *J. Micromech. Microeng.* **2001**, *11*, 287.
[266] M. Yeakub Ali, W. Hung, F. Yongqi, *Int. J. Precis. Eng. Manuf.* **2010**, *11*, 157.
[267] J. Gierak, *Semicond. Sci. Technol.* **2009**, *24*, 043001.
[268] L. A. Giannuzzi, F. A. Stevie, *Micron* **1999**, *30*, 197.
[269] N. Bassim, K. Scott, L. A. Giannuzzi, *MRS Bull* **2014**, *39*, 317.
[270] Y. Saotome, S. Okaniwa, H. Kimura, A. Inoue, *Mater. Sci. Forum* **2007**, *539–543*, 2088.
[271] F.-J. Shiou, P. H. Loc, N. H. Dang, *Int. J. Adv. Manuf. Technol.* **2013**, *66*, 1523.
[272] A. Krishnan, F. Fang, *Front. Mech. Eng.* **2019**, *14*, 299.
[273] T. Deng, J. Li, Z. Zheng, *Int. J. Mach. Tools Manuf.* **2020**, *148*, 103472.
[274] W.-L. Zhu, A. Beaucamp, *Int. J. Mach. Tools Manuf.* **2020**, *158*, 103634.
[275] C. J. Evans, E. Paul, D. Dornfeld, D. A. Lucca, G. Byrne, M. Tricard, F. Klocke, O. Dambon, B. A. Mullany, *CIRP Ann.* **2003**, *52*, 611.
[276] Z. W. Zhong, *Mater. Manuf. Processes* **2008**, *23*, 449.
[277] Z. Xia, F. Fang, E. Ahearne, M. Tao, *J. Mater. Process. Technol.* **2020**, *286*, 116828.
[278] A. P. Malshe, B. S. Park, W. D. Brown, H. A. Naseem, *Diamond Relat. Mater.* **1999**, *8*, 1198.
[279] G. Annamaria, B. Massimiliano, V. Francesco, *Int. J. Adv. Manuf. Tech.* **2022**, *120*, 1433.
[280] Z.-W. Zhong, *Mater. Manuf. Processes* **2020**, *35*, 1279.
[281] M. Frey, J. Wegner, N. Neuber, B. Reiplinger, B. Bochtler, B. Adam, L. Ruschel, S. S. Riegler, H.-R. Jian, S. Kleszczynski, G. Witt, R. Busch, *Mater. Des.* **2021**, *198*, 109368.
[282] K.-M. Hong, Y. C. Shin, *J. Mater. Process. Technol.* **2017**, *245*, 46.
[283] A. P. Mackwood, R. C. Crafer, *Opt. Laser Technol.* **2005**, *37*, 99.
[284] J. Stavridis, A. Papacharalampopoulos, P. Stavropoulos, *Int. J. Adv. Manuf. Technol.* **2018**, *94*, 1825.
[285] J. Svenungsson, I. Choquet, A. F. H. Kaplan, *Phys. Procedia* **2015**, *78*, 182.
[286] M. Dal, R. Fabbro, *Opt. Laser Technol.* **2016**, *78*, 2.
[287] X. He, *Mater. Manuf. Processes* **2012**, *27*, 1354.
[288] W. Li, A. Vairis, M. Preuss, T. Ma, *Int. Mater. Rev.* **2016**, *61*, 71.
[289] M. B. Uday, M. N. Ahmad Fauzi, H. Zuhailawati, A. B. Ismail, *Sci. Technol. Weld. Joining* **2010**, *15*, 534.
[290] D. Kumar Rajak, D. D. Pagar, P. L. Menezes, A. Eyvazian, *J. Adhes. Sci. Technol.* **2020**, *34*, 2613.
[291] M. Maalekian, *Sci. Technol. Weld. Joining* **2007**, *12*, 738.
[292] I. Bhamji, M. Preuss, P. L. Threadgill, A. C. Addison, *Mater. Sci. Technol.* **2011**, *27*, 2.

[293] G. Buffa, L. Fratini, *Prod. Eng.* **2017**, *11*, 221.
[294] M. S. Węglowski, S. Blacha, A. Phillips, *Vacuum* **2016**, *130*, 72.
[295] S. Fukushima, T. Kasugai, *Weld. Int.* **1991**, *5*, 358.
[296] S. Kagao, Y. Kawamura, Y. Ohno, *Mater. Sci. Eng., A* **2004**, *375–377*, 312.
[297] Y. Kawahito, T. Terajima, H. Kimura, T. Kuroda, K. Nakata, S. Katayama, A. Inoue, *Mater. Sci. Eng., B* **2008**, *148*, 105.
[298] Y. Kawamura, Y. Ohno, *Scr. Mater.* **2001**, *45*, 279.
[299] Y. Kawamura, Y. Ohno, *Scr. Mater.* **2001**, *45*, 127.
[300] Y. Kawamura, T. Shoji, Y. Ohno, *J. Non-Cryst. Solids* **2003**, *317*, 152.
[301] J. Kim, Y. Kawamura, *Scr. Mater.* **2007**, *56*, 709.
[302] M. Chen, D. Wei, C. Li, L. Liu, Q. Zhou, F. Wu, *Sci. Technol. Weld. Joining* **2021**, *26*, 264.
[303] S. H. Wang, P. H. Kuo, H. T. Tsang, R. R. Jeng, J. L. Lin, *Appl. Phys. Lett.* **2007**, *91*, 171902.
[304] Y. Kawamura, *Mater. Sci. Eng., A* **2004**, *375–377*, 112.
[305] E. Perim, D. Lee, Y. Liu, C. Toher, P. Gong, Y. Li, W. N. Simmons, O. Levy, J. H. Vlassak, J. Schroers, S. Curtarolo, *Nat. Commun.* **2016**, *7*, 12315.
[306] J. J. Rehr, R. Alben, *Phys. Rev. B* **1977**, *16*, 2400.
[307] D. M. C. Nicholson, G. M. Stocks, W. A. Shelton, Y. Wang, J. C. Swihart, *Metall. Mater. Trans. A* **1998**, *29*, 1845.
[308] A. Păduraru, A. Kenoufi, N. P. Bailey, J. Schiøtz, *Adv. Eng. Mater.* **2007**, *9*, 505.
[309] J. A. Reyes-Retana, G. G. Naumis, *J. Non-Cryst. Solids* **2015**, *409*, 49.
[310] X. Hui, H. Z. Fang, G. L. Chen, S. L. Shang, Y. Wang, J. Y. Qin, Z. K. Liu, *Acta Mater.* **2009**, *57*, 376.
[311] S.-P. Ju, H.-H. Huang, J. C.-C. Huang, *J. Non-Cryst. Solids* **2014**, *388*, 23.
[312] R. Atta-Fynn, D. A. Drabold, P. Biswas, *J. Non-Cryst. Solids X* **2019**, *1*, 100004.
[313] T. A. Weber, F. H. Stillinger, *Phys. Rev. B* **1985**, *31*, 1954.
[314] R. Tarumi, A. Ogura, M. Shimojo, K. Takashima, Y. Higo, *Jpn. J. Appl. Phys., Part 2* **2000**, *39*, L611.
[315] P. Ballone, S. Rubini, *Phys. Rev. Lett.* **1996**, *77*, 3169.
[316] O. Rodríguez de la Fuente, J. M. Soler, *Phys. Rev. Lett.* **1998**, *81*, 3159.
[317] Y. Qi, T. Çağın, Y. Kimura, W. A. Goddard, *Phys. Rev. B* **1999**, *59*, 3527.
[318] M. Wakeda, H. Saida, J. Li, S. Ogata, *Sci. Rep.* **2015**, *5*, 10545.
[319] F. Ren, L. Ward, T. Williams, K. J. Laws, C. Wolverton, J. Hattrick-Simpers, A. Mehta, *Sci. Adv.* **2018**, *4*, eaaq1566.
[320] J. Xiong, S.-Q. Shi, T.-Y. Zhang, *Mater. Des.* **2020**, *187*, 108378.
[321] Z. Lu, X. Chen, X. Liu, D. Lin, Y. Wu, Y. Zhang, H. Wang, S. Jiang, H. Li, X. Wang, Z. Lu, *npj Comput. Mater.* **2020**, *6*, 187.
[322] D. G. Mastropietro, J. A. Moya, *Comput. Mater. Sci.* **2021**, *188*, 110230.
[323] L. Ward, S. C. O'Keeffe, J. Stevick, G. R. Jelbert, M. Aykol, C. Wolverton, *Acta Mater.* **2018**, *159*, 102.
[324] X. Liu, Z. Long, L. Yang, W. Zhang, Z. Li, *J. Non-Cryst. Solids* **2021**, *570*, 121000.
[325] L. Ward, A. Agrawal, A. Choudhary, C. Wolverton, *npj Comput. Mater.* **2016**, *2*, 16028.
[326] H. Joress, B. L. DeCost, S. Sarker, T. M. Braun, S. Jilani, R. Smith, L. Ward, K. J. Laws, A. Mehta, J. R. Hattrick-Simpers, *ACS Comb. Sci.* **2020**, *22*, 330.
[327] A. Montoya Obeso, J. Benois-Pineau, M. S. García Vázquez, A. A. Ramirez Acosta, *Multimedia Tools Appl.* **2019**, *78*, 9553.
[328] https://www.tensorflow.org/ (accessed: October 2022).
[329] https://caffe.berkeleyvision.org/ (accessed: October 2022).
[330] https://keras.io/ (accessed: October 2022).
[331] J. Li, K. Lim, H. Yang, Z. Ren, S. Raghavan, P.-Y. Chen, T. Buonassisi, X. Wang, *Matter* **2020**, *3*, 393.
[332] W. Sha, Y. Guo, Q. Yuan, S. Tang, X. Zhang, S. Lu, X. Guo, Y.-C. Cao, S. Cheng, *Adv. Intell. Syst.* **2020**, *2*, 1900143.
[333] P. Jiao, A. H. Alavi, *Int. Mater. Rev.* **2021**, *66*, 365.
[334] K. T. Butler, D. W. Davis, H. Cartwright, O. Isayev, A. Walsh, *Nature* **2018**, *559*, 547.
[335] R. K. Vasudevan, K. Choudhary, A. Mehta, R. Smith, G. Kusne, F. Tavazza, L. Vlcek, M. Ziatdinov, S. V. Kalinin, H. Hattrick-Simpers, *MRS Commun.* **2019**, *9*, 821.
[336] C. P. Gomes, B. Selman, J. M. Gregoire, *MRS Bull.* **2019**, *44*, 538.
[337] J. S. Huang, J. X. Liew, A. S. Ademiloye, K. M. Liew, *Arch. Comput. Methods Eng.* **2021**, *28*, 3399.
[338] R. Vasudevan, G. Pilania, P. V. Balachandran, *J. Appl. Phys.* **2021**, *129*, 070401.
[339] J. F. Rodrigues, L. Florea, M. C. F. de Oliveira, D. Diamond, O. N. Oliveira, *Discover Mater.* **2021**, *1*, 12.
[340] K. Choudhary, B. DeCost, C. Chen, A. Jain, F. Tavazza, R. Cohn, C. W. Park, A. Choudhary, A. Agrawal, S. J. L. Billinge, E. Holm, S. P. Ong, C. Wolverton, *npj Comput. Mater.* **2022**, *8*, 59.
[341] E. O. Pyzer-Knapp, J. W. Pitera, P. W. J. Staar, S. Takeda, T. Laino, D. P. Sanders, J. Sexton, J. R. Smith, A. Curioni, *npj Comput. Mater.* **2022**, *8*, 84.
[342] J. Xiong, S.-Q. Shi, T.-Y. Zhang, *Comput. Mater. Sci.* **2021**, *192*, 110362.
[343] M. Samavatian, R. Gholamipour, V. Samavatian, *Comput. Mater. Sci.* **2021**, *186*, 110025.
[344] Y. X. Zhang, G. C. Xing, Z. D. Sha, L. H. Poh, *J. Alloys Compd.* **2021**, *875*, 160040.
[345] Z. Q. Zhou, Q. F. He, X. D. Liu, Q. Wang, J. H. Luan, C. T. Liu, Y. Yang, *npj Comput. Mater.* **2021**, *7*, 138.
[346] S. Feng, H. Fu, H. Zhou, Y. Wu, Z. Lu, H. Dong, *npj Comput. Mater.* **2021**, *7*, 10.
[347] T.-C. Chen, S.-Y. Yu, S. Sajjadifar, *Mater. Lett.* **2021**, *290*, 129441.
[348] A. Vabalas, E. Gowen, E. Poliakoff, A. J. Casson, *PLoS One* **2019**, *14*, e0224365.
[349] Z. Song, X. Chen, F. Meng, G. Cheng, C. Wang, Z. Sun, W.-J. Yin, *Chin. Phys. B* **2020**, *29*, 116103.
[350] J. Li, T.-C. Chen, A. Olegovna Zekiy, *Appl. Phys. A* **2021**, *127*, 720.
[351] T.-C. Chen, R. Rajiman, M. Elveny, J. W. Grimaldo Guerrero, A. I. Lawal, N. K. A. Dwijendra, A. Surendar, S. D. Danshina, Y. Zhu, *Arabian J. Sci. Eng.* **2021**, *46*, 12417.
[352] B. Deng, Y. Zhang, *Chem. Phys.* **2020**, *538*, 110898.
[353] X. Liu, X. Li, Q. He, D. Liang, Z. Zhou, J. Ma, Y. Yang, J. Shen, *Acta Mater.* **2020**, *201*, 182.
[354] R.-J. Palma-Mendoza, D. Rodriguez, L. de-Marcos, *Knowl. Inf. Syst.* **2018**, *57*, 1.
[355] J. Cai, X. Chu, K. Xu, H. Li, J. Wei, *Nanoscale Adv.* **2020**, *2*, 3115.
[356] I. T. Jolliffe, *Principal Component Analysis*, Springer, New York, NY **2002**.
[357] Z. Li, Z. Long, S. Lei, T. Zhang, X. Liu, D. Kuang, *Comput. Mater. Sci.* **2021**, *197*, 110656.
[358] M. Singla, K. K. Shukla, *Neural Comput. Appl.* **2020**, *32*, 11173.
[359] J. Bergstra, Y. Bengio, *J. Mach. Learn. Res.* **2012**, *13*, 281.
[360] S. Gil-Begue, C. Bielza, P. Larrañaga, *Artif. Intell. Rev.* **2021**, *54*, 519.
[361] P. Fernández-González, C. Bielza, P. Larrañaga, *IEEE Access* **2019**, *7*, 25660.
[362] C. Wen, Y. Zhang, C. Wang, D. Xue, Y. Bai, S. Antonov, L. Dai, T. Lookman, Y. Su, *Acta Mater.* **2019**, *170*, 109.
[363] M. Iqbal, Y. Zhu, *ICTACT J. Soft Comput.* **2015**, *5*, 946.
[364] Y. Chali, S. R. Joty, S. A. Hasan, *J. Artif. Intell. Res.* **2009**, *35*, 1.
[365] B. Jo, R. L. Findling, C.-P. Wang, T. J. Hastie, E. A. Youngstrom, L. E. Arnold, M. A. Fristad, S. McCue Horwitz, *Stat. Med.* **2017**, *36*, 671.
[366] J. Garcia, F. Fernández, *J. Mach. Learn. Res.* **2015**, *16*, 1437.

[367] S. Padakandla, *ACM Comput. Surv.* **2022**, *54*, 127.
[368] L. Peng, Z. Long, M. Zhao, *Comput. Mater. Sci.* **2021**, *195*, 110480.
[369] B. Ren, Z. Long, R. Deng, *Comput. Mater. Sci.* **2021**, *189*, 110259.
[370] L. E. Schultz, B. Afflerbach, C. Francis, P. M. Voyles, I. Szlufarska, D. Morgan, *Comput. Mater. Sci.* **2021**, *196*, 110494.
[371] T.-C. Chen, M. Elveny, A. Surendar, A. I. Lawal, A. O. Zekiy, R. Anzum, *Modell. Simul. Mater. Sci. Eng.* **2021**, *29*, 065019.
[372] R. Deng, Z. Long, L. Peng, D. Kuang, B. Ren, *J. Non-Cryst. Solids* **2020**, *533*, 119829.
[373] A. Dasgupta, S. R. Broderick, C. Mack, B. U. Kota, R. Subramanian, S. Setlur, V. Govinaraju, K. Rajan, *Sci. Rep.* **2019**, *9*, 357.
[374] J. Xiong, T.-Y. Zhang, S.-Q. Shi, *MRS Commun.* **2019**, *9*, 576.
[375] N. Islam, W. Huang, H. L. Zhuang, *Comput. Mater. Sci.* **2018**, *150*, 230.
[376] M. H. Yang, J. H. Li, B. X. Liu, *Phys. Chem. Chem. Phys.* **2017**, *19*, 16850.
[377] M. K. Tripathi, S. Ganguly, P. Dey, P. P. Chattopadhyay, *Comput. Mater. Sci.* **2016**, *118*, 56.
[378] M. K. Tripathi, P. P. Chattopadhyay, S. Ganguly, *Comput. Mater. Sci.* **2015**, *107*, 79.
[379] https://scikit-learn.org/stable/getting_started.html (accessed: October 2022).
[380] Y. Bengio, Y. Grandvalet, *J. Mach. Learn. Res.* **2004**, *5*, 1089.
[381] B. Efron, *J. Am. Stat. Assoc.* **1983**, *78*, 316.
[382] G. Jiang, W. Wang, *Pattern Recognit.* **2017**, *69*, 94.
[383] L. Breiman, *Mach. Learn.* **2001**, *45*, 5.
[384] N. Altman, M. Krzywinski, *Nat. Methods* **2017**, *14*, 933.
[385] A. Galicia, R. Talavera-Llames, A. Troncoso, I. Koprinska, F. Martínez-Álvarez, *Knowledge-Based Syst.* **2019**, *163*, 830.
[386] J. L. Speiser, B. J. Wolf, D. Chung, C. J. Karvellas, D. G. Koch, V. L. Durkalski, *Chemom. Intell. Lab. Syst.* **2019**, *185*, 122.
[387] T. Chen, C. Guestrin, in *Proc. of the ACM SIGKDD Inter. Conf. on Knowledge Discovery and Data Mining* **2016**, pp. 785–794, https://doi.org/10.1145/2939672.2939785.
[388] J. H. Friedman, *Ann. Stat.* **2001**, *29*, 1189.
[389] Y. Zhang, A. Haghani, *Transp. Res. Part C Emerging Technol.* **2015**, *58B*, 308.
[390] Z. Zhang, Z. Liu, D. Wu, *Addit. Manuf.* **2021**, *37*, 101692.
[391] O. Köksoy, *Appl. Math. Comput.* **2006**, *175*, 1716.
[392] D. M. Allen, *Technometrics* **1971**, *13*, 469.
[393] C. Toro-Vizcarrondo, T. D. Wallace, *J. Am. Stat. Assoc.* **1968**, *63*, 558.
[394] A. C. Cameron, F. A. G. Windmeijer, *J. Bus. Econ. Stat.* **1996**, *14*, 209.
[395] X. Wang, B. Jiang, J. S. Liu, *Biometrika* **2017**, *104*, 129.
[396] K. Gao, X. G. Zhu, L. Chen, W. H. Li, X. Xu, B. T. Pan, W. R. Li, W. H. Zhou, L. Li, W. Huang, Y. Li, *J. Mater. Sci. Technol.* **2022**, *131*, 115.

Olivia A. Graeve is the Jacobs Family Professor in the Department of Mechanical and Aerospace Engineering, Director of the CaliBaja Center for Resilient Materials and Systems, and Director of the Materials Science and Engineering Program at UC San Diego. Her area of research focuses on the design and processing of new materials for extreme environments. She has been involved in many activities related to the recruitment and retention of women and underrepresented students in science and engineering and has received several prestigious awards including the Presidential Award for Excellence in Science, Mathematics and Engineering Mentoring in 2020.

Mireya Saraí García Vázquez received her Ph.D. in signals and telecommunications from the University of Rennes, France. She completed her postdoctoral studies at the PILIMTEC R&D laboratory in Brest, France, and subsequently completed a residence as a Fulbright Scholar at San Diego State University. She is currently a professor at the Digital Technology Research and Development Center of the Instituto Politécnico Nacional (IPN). Her area of expertise is in deep learning for applications in materials science and multimedia indexing. This year, she was awarded the IPN Research Award for her outstanding contributions to technology development.